Plasmonic Metasurfaces

Submitted by

Asad Ahmad Tahir

(June 2016)

Supervisor: Robert W. Boyd

A thesis submitted in partial fulfilment of the requirements
for the degree of Masters of Applied Science in
Electrical and Computer Engineering

Faculty of Graduate Studies
University of Ottawa
Ottawa, Ontario, Canada

Abstract

Nanophotonics is a booming field of research with the promise of chip-scale devices which harness the tremendous potency of light. In this regard, surface plasmons have shown great potential for confining and manipulating light at extreme sub-wavelength scales. Advances in fabrication technology have enabled the scientific community to realize metasurfaces with unconventional properties that push the limits of possible applications of light. This thesis is comprised of computational and experimental studies on plasmonic metasurfaces. The computational study presents efficient design principles for plasmonic half-wave plates using L-shaped nanoantennas. These principles can be used to design waveplates at an operating wavelength of choice and for specific application requirements. The impact of this study goes beyond the efficient design of waveplates: it provides useful insights into the Physics of L-shaped nanoantenna arrays which have been proposed as building blocks for plasmonic metasurfaces. The experimental work investigates the interaction of a plasmonic metasurface, composed of dipole antenna arrays, with an epsilon-near-zero (ENZ) material. This work thus forms a bridge between plasmonics and ENZ materials science, which is a rapidly advancing field in its own right. The first experimental study investigates the exciting unconventional response of plasmonic dipole antennas when placed on a thin indium tin oxide (ITO) film near its ENZ wavelength of 1417 nm. The antenna-on-ITO system has split resonances whose spectral positions are largely independent of the antenna dimensions. The resonance splitting occurs due to coupling between the antenna resonance and the ENZ mode of the ITO film. This coupling results in field intensity enhancements on the order of a 100 in the ITO film. The second experimental study demonstrates, using the z-scan method, that this large field enhancement in the antenna-on-ITO structure further enhances the already strong nonlinearity of ITO around its ENZ wavelength. In particular, the antenna-on-ITO structure exhibits an extremely large nonlinear absorption coefficient, which is two orders of magnitude larger than that of a bare ITO film, and three to five orders of magnitude larger than that of many other nonlinear materials. This thesis thus constitutes a beautiful blend of three thriving areas of research: plasmonics, ENZ materials science and nonlinear optics. The findings reported here have the potential to contribute to all of these fields, and thus have relevance to a broad spectrum of optical scientists.

Statement of originality and collaborative contributions

To the best of the author's knowledge, the three projects described in this Master's thesis are comprised of original research in Photonics. The following paragraphs describe the contribution of each participant in the project.

Chapter 2 describes a study on design principles for half-wave plate metasurfaces using plasmonic L-shaped nanoantennas. The idea was conceived by Dr. Israel De Leon, who was a postdoctoral fellow in Professor Robert W. Boyd's group. Asad Ahmad Tahir performed the simulations, conducted analysis and derived effective design principles. Dr. Sebastian Andreas Schulz[1], a postdoctoral fellow in Professor Boyd's group, and Dr. De Leon contributed with useful discussions and guidance.

Chapter 3 describes a study on the unconventional linear optical response of plasmonic dipole antennas on a thin indium tin oxide (ITO) film. The project was motivated by the discovery of the extraordinarily large nonlinearity of ITO around its epsilon-near-zero wavelength. This discovery was made by Muhammad Zahirul Alam[2], a PhD student in Professor Boyd's group. Asad A. Tahir designed and performed the experiment. He also conducted simulations to support and understand the experimental results. Dr. De Leon provided guidance for the experimental work. Dr Schulz fabricated the nanoantenna structure and took the lead role in designing simulations. All authors participated in discussions during various steps of the project. This chapter includes a simulation result obtained by Dr. Schulz, and a mode dispersion curve obtained by M. Z. Alam.

Chapter 4 describes a study on the nonlinear optical response of plasmonic dipole antennas on a thin ITO film. The project is in progress at the time of writing this thesis. M. Zahirul Alam is the principal investigator of this project. He conceived the idea and designed the experiment. Asad A. Tahir joined M. Zahirul Alam in this project and assisted with measurements as well as data analysis.

Professor Boyd supervised all aspects of these projects and contributed with useful discussions.

Table of contents

List of Figures

Chapter 1

Introduction

The guiding motivation of optical scientists is to explore ways to manipulate the properties of light for useful applications. In a world where space is a valuable asset, one of the prime objectives of scientists and engineers has been to develop devices at nanoscopic scales. The invention of the transistor has made this dream a reality and has revolutionized the world we live in. In the same vein, there has been a profound interest among Photonics scientists to develop capabilities to manipulate light at the nanoscale. This has paved the way for tremendous research activity in a field now known as *Nanophotonics* [1]. A fundamental challenge in controlling and manipulating light at nanoscopic scales is posed by the diffraction limit of light [2], due to which light in dielectric media cannot be confined within regions much smaller than the wavelength.

Maxwell's theory shows that electromagnetic energy can be confined to extreme subwavelength scales in the form of transverse magnetic (TM) surface waves on an interface between a dielectric and a medium with a negative value of the real permittivity. Metals have negative real permittivity below their plasma frequency w_p, and thus they can guide TM surface waves on an interface with a dielectric. These waves are known as *surface plasmon polariton* (SPP) modes [3].

Plasmons are collective oscillations of electrons in a metal, and the term 'polariton' is used to describe a coupled state between a photon and an elementary excitation in matter. Hence a SPP mode is an electromagnetic surface wave which arises due to the coupling of the electromagnetic field to the collective oscillations of the electron plasma of the metal. The extreme sub-wavelength confinement of SPP modes makes them promising to achieve nanoscopic manipulation of light, and has resulted in the birth of a new field of research known as *Plasmonics*.

1.1 Background

Consider the simple case of a planar interface between a metal and a non-absorbing dielectric, as shown in Figure 1.1. The dielectric has a positive and real relative permittivity ε_d, whereas the metal has a relative permittivity given by ε_m. We would like to solve for a guided TM mode (the SPP mode) which is confined around the interface, i.e which propagates along the x direction and decays in the z direction. We can define the TM field we are solving for as

$$\vec{H}_y = \hat{y}\, H_0 e^{ik_x x} \begin{pmatrix} e^{-\alpha_d z} \text{ for } z \geq 0 \\ e^{\alpha_m z} \text{ for } z < 0 \end{pmatrix}, \tag{1.1}$$

where k_x, the propagation constant, is the component of the wavevector in the direction of propagation.

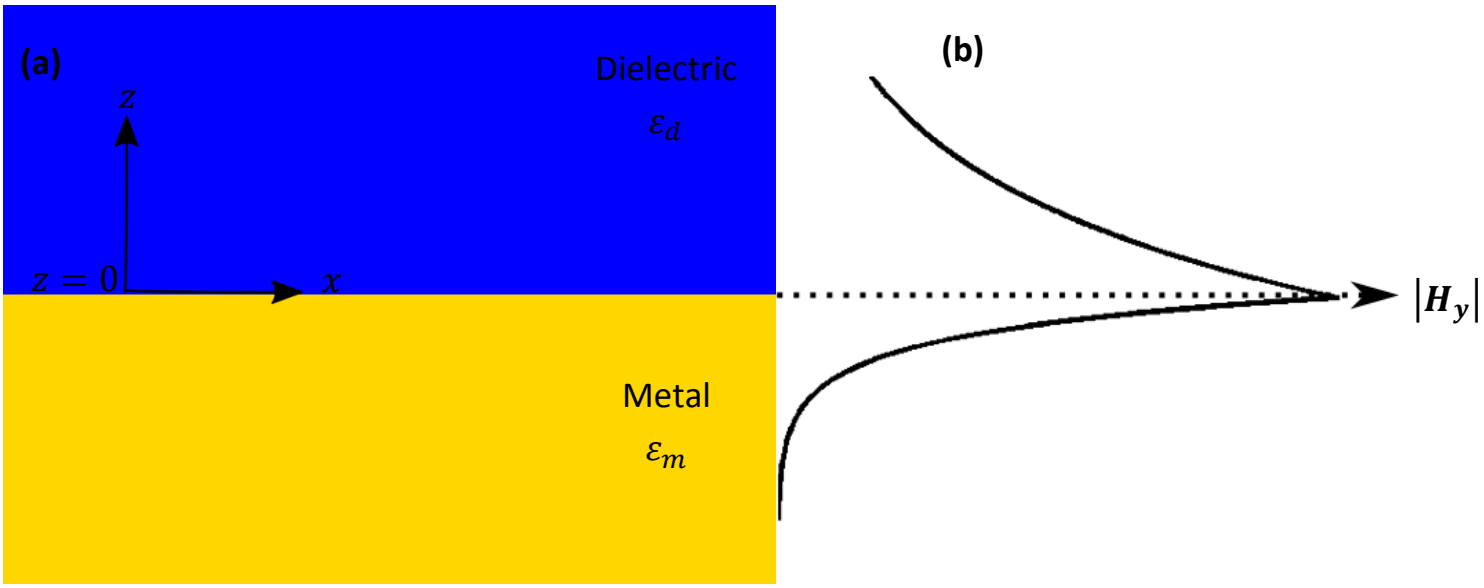

Figure 1.1: (**a**) Metal-dielectric interface which can support a SPP mode propagating along the x direction and decaying in the z direction. The coordinate axis is a right-handed system. Hence positive $\vec{H}_y$ points into the paper. (**b**) The field distribution about the interface. The field has a maximum magnitude at the interface and decays away from it.

The decay constants α_d and α_m are components of the wavevector perpendicular to the interface in the dielectric and the metal respectively. Due to the way we have defined the field in Equation (1.1), the real parts of both α_d and α_m are positive.

The equations describing the field components of the TM mode are given by [3]

$$\frac{\partial^2 H_y}{\partial z^2} + ({k_0}^2 \varepsilon - {k_x}^2) H_y = 0 \,, \tag{1.2}$$

$$E_x = -i \frac{1}{w \varepsilon_0 \varepsilon} \frac{\partial H_y}{\partial z} \,, \text{and} \tag{1.3}$$

$$E_z = -\frac{k_x}{w \varepsilon_0 \varepsilon} H_y \,, \tag{1.4}$$

where k_0 is the free space propagation vector and ε is the relative permittivity of the medium.

Maxwell's equations require that the magnetic field be continuous across an interface. Moreover, in the absence of unbound surface charge, the normal component of the electric displacement vector must also be continuous across the interface. This entails, for the particular mode we are solving for, that H_y and εE_z be continuous across the interface between the dielectric and the metal. Applying these conditions to Equations (1.3) and (1.4), we get

$$\frac{\alpha_d}{\alpha_m} = -\frac{\varepsilon_d}{\varepsilon_m} \tag{1.5}$$

Equation (1.5) clearly indicates that if ε_d is positive, then the real part of ε_m must be negative. Hence, a SPP mode can only be guided at an interface between media having opposite signs of the real part of the permittivity, i.e at an interface between a conductor and an insulator.

Moreover, H_y in Equation (1.1) has to satisfy Equation (1.2) in each medium, which yields

$$\alpha_d{}^2 = k_x{}^2 - (k_0)^2\varepsilon_d \text{ and} \tag{1.6}$$

$$\alpha_m{}^2 = k_x{}^2 - (k_0)^2\varepsilon_m \tag{1.7}$$

Equations (1.5) – (1.7) can now be used to yield

$$k_x = k_0\sqrt{\frac{\varepsilon_d\varepsilon_m}{\varepsilon_d + \varepsilon_m}} \tag{1.8}$$

Equation (1.8) is a key result that describes the dispersion relation of the SPP mode. In general, the dielectric constant ε_m and the propagation vector k_x are complex quantities.

The frequency dependence of ε_m is described by the Drude model, which treats the metal as a free electron gas. For important metals in plasmonics such as gold and silver, the model breaks down in the visible frequency range due to inter-band transitions. However, it does work well for frequencies up to the near infrared. The model describes the frequency dependence of the metal permittivity as

$$\varepsilon_m = \left(1 - \frac{w_p{}^2}{w^2 + i\Gamma w}\right), \tag{1.9}$$

where w is the frequency and Γ is the collision rate of the oscillating electrons. These collisions damp the oscillation of the free electron gas, and the collision frequency Γ is related to the relaxation time τ of the electron gas by $\Gamma = \frac{1}{\tau}$. For simplicity, if we model our metal as a free-electron gas, i.e $\Gamma \to 0$, then Equation (1.6) becomes

$$\varepsilon_m = 1 - \frac{w_p{}^2}{w^2} \tag{1.10}$$

Figure 1.2 shows the dispersion relation for a metal-glass interface, where the metal is modelled as a free electron gas. The frequency and wavevector are both normalized to the plasma frequency.

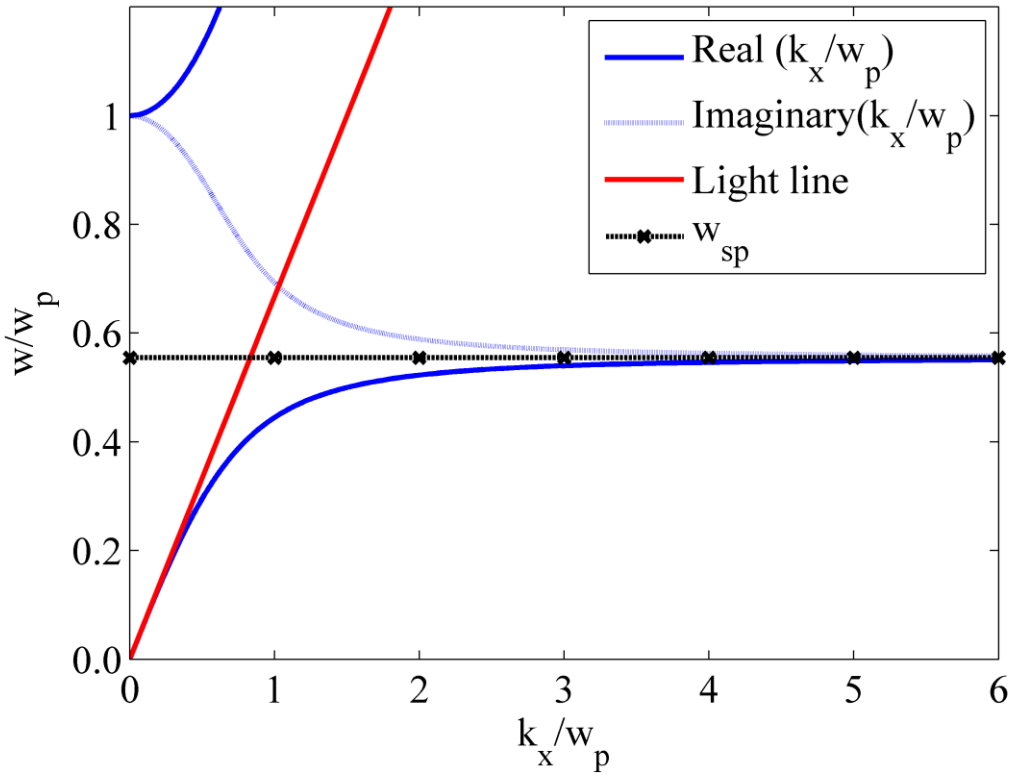

Figure 1.2: The dispersion curve of the surface plasmon polariton mode at a metal-glass interface.

The regime where k_x becomes large is particularly interesting. Equations (1.6) – (1.7) show that for large k_x, the field decay constants α_d and α_m become large and thus the SPP mode becomes highly confined. Moreover, Figure 1.2 shows that for large k_x the dispersion curve flattens out. Hence, both the phase and group velocities go to zero. Therefore, in addition to being highly confined in this regime, the mode is also highly 'localized'. The mode acquires an

electrostatic character known as *surface plasmon* [3]. We note from Equation (1.8) that the regime where k_x is large corresponds to the condition

$$\varepsilon_m + \varepsilon_d = 0 \tag{1.11}$$

The frequency w_{sp} which corresponds to the electrostatic surface plasmon resonance condition can thus be derived by substituting ε_m from Equation (1.10) into Equation (1.11), and is given as

$$w_{sp} = \frac{w_p}{\sqrt{1 + \varepsilon_d}} \tag{1.12}$$

The dispersion curve shows that between $w = w_{sp}$ and $w = w_p$, k_x is purely imaginary. This frequency region acts like a bandgap within which no propagation of the SPP mode is allowed. Consequently, the eigenfrequencies of the SPP mode range from $w = 0$ to $w = w_{sp}$. Another important aspect is that the SPP dispersion curve, except at very small k_x values, lies below the *light line* (the dispersion curve of light waves) as shown in Figure 1.2. This means that the SPP mode is non-radiative, i.e, it cannot couple directly to free-space propagating light (or light propagating in a dielectric medium) due to momentum mismatch. While this non-radiative nature of the mode is conducive for field confinement, it also means that the mode cannot be excited through direct coupling to free-space light. Consequently, special coupling mechanisms are needed to excite SPP modes. Such mechanisms include using prisms, gratings, highly focused optical beams and near-field excitation [3]. Finally, we note that for $w > w_p$, k_x becomes purely real again but the mode is now radiative, i.e, the mode can directly couple to free-space light. The metal now behaves like a lossless dielectric.

As a final comment on SPP modes on a planar metal-dielectric interface, we note that the dispersion relation in Figure 1.2 assumed an ideal conductor ($\Gamma = 0$). For real conductors, Γ is finite and hence ε_m is complex. The consequence of this is that k_x is now complex; the SPP mode attenuates as it propagates. This is of great significance since metals are lossy and greatly

inhibit the propagation length of SPPs. We also note that in addition to losses due to material absorption, SPPs also suffer from losses due to scattering.

Another consequence of a complex ε_m is that there is a finite maximum wavevector k_x at w_{sp}, as opposed to the case of the ideal conductor where k_x could become indefinitely large. This puts an upper bound on α_d and α_m, and hence on the maximum mode confinement. In fact, there is a tradeoff between the propagation length and the maximum mode confinement of the SPP mode. For more details on this the reader is referred to Reference [3].

1.2 Surface plasmon polariton modes in thin films

In addition to planar metal-dielectric interfaces, SPPs can also be supported in infinitely wide films sandwiched between other media: either a metallic film between dielectric media or a dielectric film between metallic media. When the film is thick enough such that the SPP modes on each interface do not interact, each interface supports SPP modes with properties similar to those at a metal-dielectric interface. However, when the thickness of the film is less than the skin depth, the SPP modes at each interface couple and give rise to a rich set of modes [3]. For instance, in the simple but interesting case of identical media surrounding a metal film (a symmetric film structure), the lowest order SPP mode splits into guided modes known as symmetric and asymmetric modes. These are named according to the symmetry of the electric field profile of each mode with respect to the center of the film.

The symmetric mode has the attribute that for decreasing film thickness, the amount of energy confined in the film reduces. This decreases the losses and hence the attenuation of the mode in the metal film, and consequently increases the propagation length drastically, thereby giving this mode the name long-range surface plasmon polariton [4]. This attribute is of prime importance in plasmonics since, as noted in the previous section, SPP modes generally suffer from poor propagation lengths. Long-range SPPs have thus found applications in a lot of diverse areas including nonlinear optics and biosensors [4].

On the contrary, the asymmetric mode becomes more confined to the metal film with decreasing film thickness. Consequently, their attenuation is more profound and they propagate only a short distance, prompting them to be referred to as a short-range SPP mode [5]. The

extremely high confinement of the asymmetric mode makes them very attractive for integrated photonics applications. Thus short-range SPP modes have found applications in a large variety of nanostructure configurations [5].

In asymmetric metal films (metal films sandwiched between dissimilar dielectric media), the symmetric and asymmetric modes are "symmetric-like" and "asymmetric-like" [6]. However, they are still referred to as symmetric and asymmetric modes respectively. These modes show the same trend of mode confinement to the metal with decreasing film thickness as for the symmetric film case. However, in the asymmetric film structure, the symmetric mode has a cut-off thickness: it ceases to exist below a certain thickness of the guiding film. However, the asymmetric mode (short-range SPP) has no cut-off condition [6]. This attribute adds to the promise of using short-range SPP for ultrathin, highly integrated nanophotonic structures.

1.3 Localized surface plasmons

In the previous sections we described surface plasmon polaritons, which are propagating electromagnetic surface waves, with sub-wavelength confinement, at planar metal-dielectric interfaces. Another fundamental plasmonic excitation occurs in sub-wavelength metal nanostructures, and constitutes non-propagating oscillations of the conduction electrons coupled to the electromagnetic field. These are known as *localized surface plasmons* (LSPs) [3]. These, due to being localized to the nanostructure, are not described by a wavevector. Consequently, unlike SPP modes, LSP modes do not need special coupling mechanisms to be excited by free-space light.

LSPs are attractive because, under resonant excitation, they produce huge field enhancements inside and in the close proximity of the nanostructure. This has applications, for instance, to plasmonic printing for photofabrication of nanostructures, surface-enhanced raman scattering, enhancement of nonlinear optical effects and apertureless near-field microscopy and spectroscopy [7]. Moreover, nanostructures scatter strongly at the LSP resonance, enabling to use them as so-called "nanoantennas" for several applications [8].

The LSP resonance of a nanostructure is directly related to its polarizability: the LSP resonance, and hence the field enhancement and strong scattering, occurs when there is a resonant enhancement in the polarizability of the nanostructure. The spectral response of the

polarizability, in turn, depends on the permittivity of the surrounding environment. This has had huge applications to using nanostructures, which support LSP resonance, as sensors for detecting changes in the refractive index of their environment [9]. Due to the strong field localization of LSP resonances, these LSP sensors can detect localized refractive index changes within nanoscopic regions. They can thus be used to study molecular interactions in close proximity of the sensor.

Furthermore, the polarizability of the nanostructure also depends on its geometric and material properties. This provides flexibility to design nanostructures that afford field-enhancement and strong scattering properties at desired wavelengths. As an example of this, we note that the polarizability p, field enhancement E_{enhance} and scattering crossection C_{sca} for a sphere of radius a in the quasi-static approximation $\left(a < \frac{\text{Incident wavelength}}{10}\right)$ are given by [3]

$$p = 4\pi a^3 \frac{\varepsilon - \varepsilon_{\text{sphere}}}{\varepsilon + 2\varepsilon_{\text{sphere}}}, \tag{1.13}$$

$$E_{\text{enhance}} = \frac{E_{\text{in}}}{E_0} = \frac{3\varepsilon_{\text{sphere}}}{\varepsilon + 2\varepsilon_{\text{sphere}}}, \text{and} \tag{1.14}$$

$$C_{\text{sca}} = \frac{k^4}{6\pi} |p|^2, \tag{1.15}$$

where $\varepsilon_{\text{sphere}}$ and ε are the relative permittivities of the sphere and a lossless, isotropic surrounding medium, E_0 is the incident field with wavenumber k, and E_{in} is the induced field inside the sphere. We see that at the resonance condition of p, i.e $\varepsilon + 2\varepsilon_{sphere} \to 0$, both the induced field E_{in} and the scattering crossection C_{sca} are enhanced.

For a detailed theoretical treatment demonstrating the relationship between structure properties, polarizability, field enhancement and scattering, the reader is referred to Reference [3]. It is important to note that analytical expressions for polarizability can be derived for only a few geometries. However, since full vectorial wave solutions such as the Finite Difference Time

Domain method are available, this does not pose a bottleneck for designing arbitrary nanostructures.

1.4 Nanoantennas as Fabry-Perot cavities

Nanoantennas should not only be good scatterers, but should also afford strong field enhancements to realize the vast potential of LSP resonances as discussed above. In this regard, bar-like nanoparticles have the potential to be good nanoantennas [8]. From the point of view of designing such nanoantennas, analytically calculating the polarizability can be difficult. This is especially true for more complex structures made from these bar-like antennas such as L-shaped antennas. A convenient and widely used method to work around this difficulty is to treat bar-like antennas as Fabry-Perot cavities, whose LSP resonances for light polarized along their long-axis are given by [7]

$$L = \frac{n}{2}\lambda_{\text{eff}}\,, \tag{1.16}$$

where L is the length of the antenna, n is any positive integer which corresponds to the order of the resonance, and λ_{eff} is the effective wavelength [8].

We would like to clarify here that the LSP resonance is not described by a wave-vector. The wave-vector corresponding to λ_{eff} in Equation (1.13) is an effective wave-vector in the phenomenological picture of treating bar-like antennas as Fabry-Perot cavities. The validity of this approach has been verified in previous works, such as in [8].

In this thesis, we are interested in the lowest order resonance where, analogous to radio frequency antennas, the nano-bar acts like a half-wave dipole antenna and supports dipolar current distributions. In Chapter 2, we will be concerned with the lowest order resonances of L-shaped nanoantennas, whose resonance conditions are described by the Fabry-Perot phenomenological picture described here.

1.5 Plasmonic metasurfaces

Individual nanoparticles in general can be designed to give properties not found in natural materials. These individual nanostructures can thus serve to go "beyond" ("meta" in Greek) what is achievable with natural materials: they can serve as meta-atoms. An example of this is the birefringent plasmonic L-antenna discussed in Chapter 2. Owing to their sub-wavelength size, the scattering crossection of individual nanoparticles is often too weak for practical applications. Consequently, a large number of these nanoparticles is required to obtain a strong response. Since it is easier to fabricate planar structures, metasurfaces comprising of several individual meta-atoms arranged in planar arrays have been quite popular. In particular, plasmonic metasurfaces is an active field of research [10].

The scope of this thesis is to study two specific plasmonic metasurfaces which harbor exciting properties. In this chapter we have reviewed fundamental concepts relevant to the forthcoming chapters. In chapter 2, we present a study on the design principles for half-wave plate metasurfaces using plasmonic L-shaped nanoantennas. This study provides useful insights into the Physics of L-shaped nanoantenna arrays, which have been proposed as building blocks for plasmonic metasurfaces.

Our research group discovered that indium tin oxide (ITO) exhibits a large optical nonlinearity around its epsilon-near-zero (ENZ) wavelength. This motivated us to investigate the interaction of plasmonic structures with a thin ITO film near its ENZ wavelength. In chapter 3, we study the anomalous linear optical response of plasmonic dipole antenna arrays on a thin ITO film. This study demonstrates an exciting union of plasmonics and ENZ materials science. In chapter 4, using structures similar to the ones studied in chapter 3, we show how plasmonic dipole antennas can greatly enhance the already strong nonlinear optical response of ITO. We conclude by discussing the relevance of this thesis in the broader context of Photonics.

Chapter 2

Design principles for half-wave plate metasurfaces using plasmonic L-shaped nanoantennas

2.1 Introduction

Half-wave plates are optical elements which introduce a π phase shift between two orthogonal polarizations of incident light. By virtue of this, they are able to rotate the polarization vector of linearly polarized light, as well as invert the handedness of elliptically polarized light. In addition to their conventional applications to polarization rotation, they have had more recent applications to geometric phase elements such as the q-plate [10]. With the advent of nanophotonics, there has been an increasing interest in manipulating the phase and polarization of light at the nanoscale using surface plasmons [12-22]. As such, substantial work has been done in realizing plasmonic waveplates, often using structures that support two orthogonal plasmonic eigenmodes [13-20]. The symmetry axes of these eigenmodes play the role of the principal axes of birefringent media used to make conventional wave plates. They are thus tailored to scatter light with equal amplitude and an appropriate phase difference, such as π for a half-wave plate, at the desired excitation wavelength. However, due to the finite linewidth of these eigenmodes, plasmonic waveplates often have a limited bandwidth. They traditionally also have low efficiencies due in part to inherent dissipative effects in plasmonic structures. The best reported half-wave plate efficiency for singe-layered planar plasmonic structures less than 100 nm thick is 20% [26]. More recently though, multilayered plasmonic structures have been demonstrated that work as broadband and highly efficient waveplates and are well suited for applications that work in reflection [31-34]. However, working in reflection is not suitable for all applications.

A structure of considerable interest for ultrathin, single-layered plasmonic metasurfaces is the L-shaped nanoantenna. It supports two orthogonal eigenmodes, which are identified in Figure 2.1 as the symmetric mode and the antisymmetric mode. The symmetric mode is excited by light polarized along the symmetric axis and supports dipolar currents along each arm of the antenna. The antisymmetric mode is excited by light polarized along the antisymmetric axis and supports dipolar currents which span across both arms of the antenna. The eigenmodes introduce

a phase shift Φ between the incident and scattered fields across their resonance. The phase difference, ΔΦ, between the fields scattered from the eigenmodes peaks between their resonance centers, hitherto referred to as the overlap region and shaded grey in Figure 2.1e. Hence the spectral gap between the resonances affects the width and magnitude of the ΔΦ profile.

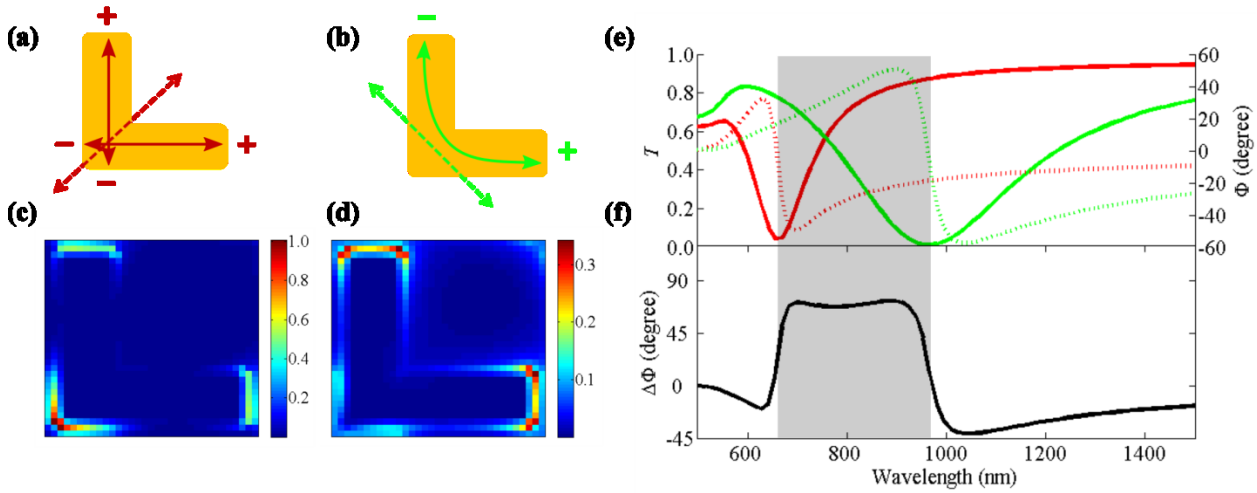

Figure 2.1: The excitation axis (dotted arrow) and dipolar currents (solid arrows) for the **(a)** symmetric mode and the **(b)** antisymmetric mode. The field intensity distribution on an individual antenna, normalized to the intensity distribution of the symmetric mode, for the **(c)** symmetric eigenmode and the **(d)** antisymmetric eigenmode. **(e)** Transmission spectrum *T* (solid line) and phase Φ (dotted) of symmetric (red) and antisymmetric (green) eigenmode. **(f)** The phase difference ΔΦ between light scattered from each eigenmode.

The anisotropy of these antennas was first demonstrated by Xu et.al [35], and it has been used to realize waveplates [36-38], phased arrays [39] and plasmonic q-plates [40-41]. Theoretical models for the amplitude and phase response of these antennas have been proposed. However, these consider a thin-wire approximation [42], which is not always accurate for 'fat' antennas having a small ratio of arm length to width. Moreover, they do not consider strong coupling between antennas in an array [42-43]. In order to study the response of these antenna arrays while fully utilizing their vast parameter space, a full vectorial wave solution such as the Finite Difference Time Domain method (FDTD) [44] is required. However, due to the fine mesh resolution required to accurately model plasmonic structures, designing ultrathin plasmonic waveplates using the vast parameter space of L-shaped nanoantennas can be time consuming.

In this work, we report principles to design periodic arrays of L-shaped nanoantennas to realize plasmonic half-wave plates in transmission. The principles we present can be used to design quickly at a desired wavelength region for specific application requirements and available fabrication processes. The parameter space we explore in this work includes the length L and width w of each arm of the antenna, the lattice period P and the array topology quantified by angle θ as shown in Figure 2.2. Since practical plasmonic waveplates require arrays of nanostructures, the array parameters are an important parameter to explore.

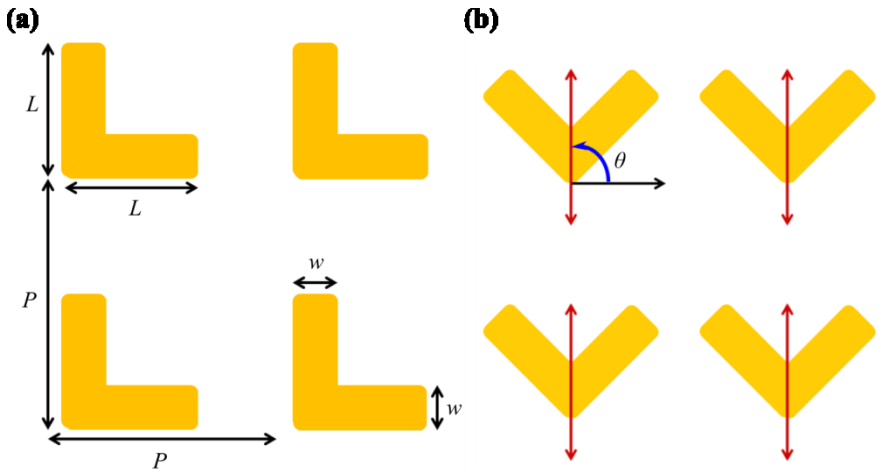

Figure 2.2: The parameters we consider for our study. **(a)** The arm length L, the arm width w, and the period P. **(b)** Array topology quantified by angle θ from horizontal to symmetric axis (red arrow).

2.2 Method of analysis

We use Lumerical FDTD solutions [45], a commercial FDTD solver, for our investigation. The structure we consider is a two-dimensional periodic array of 40-nm-thick gold antennas on a semi-infinite glass substrate, where the dielectric constants of the gold and glass are taken from [46] and [47] respectively. The angle between the antenna arms is fixed at 90˚. In our simulations, a mesh step of $\Delta x = 5$ nm, $\Delta y = 5$ nm and $\Delta z = 3$ nm is used for the span of the antenna. These settings provide mesh convergence within 1% for transmission and within 7% for resonance wavelength. The mesh convergence was calculated against a mesh step of $\Delta x = 2$ nm, $\Delta y = 2$ nm and $\Delta z = 2$ nm for the span of the antenna, and was performed for a specific array

with dimensions P = 200 nm, L = 140 nm, w = 40 nm and θ = 45°. We thus used the stated mesh settings for faster computation. Since half-wave plates invert the handedness of incident circularly polarized light, we assess the performance of our designs in transmission by defining as follows the purity ρ, the transmission T and the efficiency η for a right circularly polarized plane wave input at normal incidence

$$\rho = \frac{Left\ Circularly\ Polarized\ Scattered\ Power}{Total\ Scattered\ Power}, \tag{2.1}$$

$$T = \frac{Total\ Scattered\ Power}{Incident\ Power}, \text{and} \tag{2.2}$$

$$\eta = \frac{Left\ Circularly\ Polarized\ Scattered\ Power}{Incident\ Power} = \rho \text{ x } T \tag{2.3}$$

The purity ρ depends on both the scattering power and phase of each eigenmode, and equals 1 when the relative powers are equal and the phase difference is π. For each design, we ran separate simulations with the source polarized along each eigenmode axis of the antenna. The fields transmitted by the array were recorded at a two-dimensional monitor placed 4.0 μm above, and parallel to, the plane of the antenna array. A perfectly matched layer (PML) boundary was placed 4.2 μm above the antenna array. The monitor was placed this far above the array in order to have a highly uniform field profile on the monitor surface, thereby allowing us to use the average of the field on the monitor and therefore simplify the subsequent calculations. We combined the field components with the appropriate phase shift to calculate the equivalent response to a right circularly polarized input. We then projected the polarization of the combined response on left circular polarization to calculate ρ and the efficiency η. The details regarding implementation of this procedure, provided in the supplementary section at the end of this chapter, illustrate a strategy to save valuable computation time through applying fundamental concepts.

In the following sections, we discuss the impact of varying the design parameters on ρ and η.

2.3 Effect of varying the parameters

For the following discussion, we define the array fill-factor as the percentage of the planar array area occupied by the antennas. The topology parameter θ is set to 45˚ unless noted otherwise. We divide the discussion of the effect of varying each parameter into two domains, depending on the strength of inter-antenna coupling, which critically depends on the inter-antenna spacing. We define the weak coupling domain, within which changing P does not significantly shift the resonance wavelength of each eigenmode, and the strong coupling domain, where the resonance wavelengths do shift by changing P. We also assume that $\Delta\Phi$ is smaller than π.

In the following, the transmission spectrum of symmetric resonance is shown in red, and that of the antisymmetric resonance is shown in green.

2.3.1 Effect of increasing the period *P*

In the weak coupling domain, increasing P does not significantly shift the resonance wavelength of the eigenmodes as shown in Figure 2.3. Hence the $\Delta\Phi$ and ρ profiles do not spectrally shift. Since the inter-antenna coupling weakens due to the increased inter-antenna spacing, the damping is reduced and the resonance linewidth narrows. Consequently the phase shift imparted by each eigenmode is reduced in the overlap region, reducing $\Delta\Phi$ and hence ρ, as shown in Figure 2.3(b) – 2.3(c). Moreover, the width of the $\Delta\Phi$ profile remains the same, since it depends on the spectral gap between the eigenmodes. Hence the width of the ρ profile does not change significantly either.

In the strong coupling domain, however, increasing P does not only reduce the damping. It also results in a blue-shift of the resonance wavelength towards those of the isolated antenna [48], due to the strong near-field coupling present in this regime, thereby blue-shifting $\Delta\Phi$ and ρ. We observe that the symmetric resonance blue-shifts more than the antisymmetric one. This is because the symmetric resonance has stronger fields on the corners of the antenna, as shown in Figure 2.1(c), and hence is more strongly coupled to the neighbouring antennas. The discrepancy

in the spectral shift of each resonance increases the spectral gap between them, and thus broadens and reduces $\Delta\Phi$ and ρ as shown in Figures 2.3(f) and 2.3(g). Moreover, the resonances become narrower which also contributes to reducing $\Delta\Phi$ and ρ.

For very small inter-antenna gaps, the resonances are very broad due to very strong inter-particle coupling. This results in a larger phase difference and purity. Consequently, the strong coupling domain, in general, affords a larger ρ as compared to the weak coupling domain.

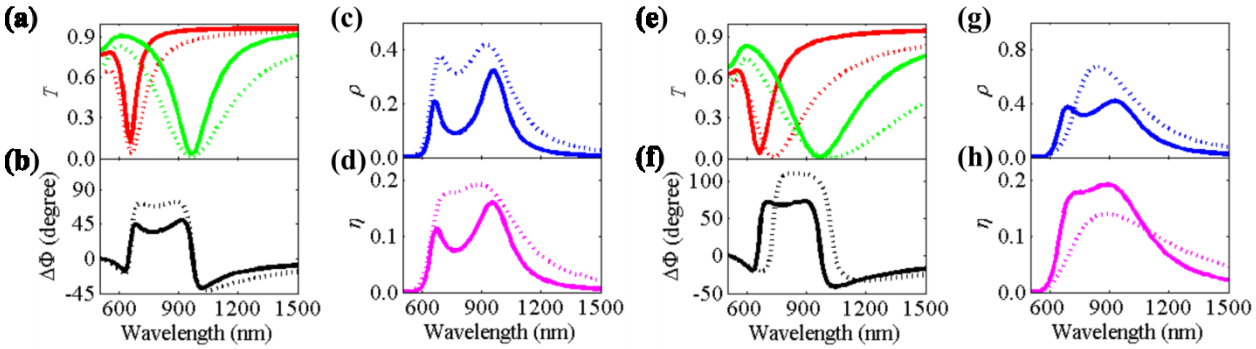

Figure 2.3. **(a)-(d)**: Effect of increasing period in weak coupling domain. T, $\Delta\Phi$, ρ and η are shown for P = 200 nm (dotted lines) and P = 280 nm (solid lines). Other antenna dimensions are L = 140 nm, w = 40 nm. Each resonance narrows but its central wavelength does not change. Consequently the width of $\Delta\Phi$, ρ and η does not change. Due to narrower resonance, $\Delta\Phi$ and hence ρ reduces. **(e)-(h)**: Effect of increasing period in strong coupling domain. T, $\Delta\Phi$, ρ and η for P = 160 nm (dotted lines) and P = 200 nm (solid lines). Other antenna dimensions are L = 140 nm, w = 40 nm. Increasing the period blueshifts the symmetric eigenmode more than the antisymmetric one, thereby increasing the spectral spacing between the two resonance centers. The resonances become narrower as well. Both of these effects reduce $\Delta\Phi$ and hence ρ.

2.3.2 Effect of increasing the antenna's arm length *L*

In either domain, increasing the arm length L gives rise to two contrary effects on the phase difference $\Delta\Phi$ and hence the purity ρ. Since the resonances scale with arm length [39], increasing L redshifts the resonances. Consequently, both $\Delta\Phi$ and ρ redshift. Since the antisymmetric eigenmode spans across both arms of the antenna, whereas the symmetric eigenmode spans across one, the antisymmetric resonance redshifts more than the symmetric one (Figure 2.4). Hence the spectral spacing between these resonances increases, which reduces and broadens $\Delta\Phi$ and ρ in the overlap region. However, a larger L reduces the inter-antenna spacing,

which broadens the resonances and thus increases ΔΦ. These are competing effects, and thus the net change in ΔΦ and ρ in the overlap region will depend on which effect will dominate.

In the strong coupling domain we observe that, for the same increase in L, each eigenmode redshifts more as compared to its redshift in the weak coupling domain. This is because in the strong coupling domain, the stronger near-field coupling due to the increase in L also contributes to redshifting the resonances. As explained earlier, the near-field coupling shifts the symmetric resonance more than the antisymmetric one. Therefore, the increment in the spectral spacing between the resonances is less pronounced as compared to that for the weak coupling domain. Hence, the negative contribution to the phase difference ΔΦ and the purity ρ due to increase in inter-resonance spectral spacing is less profound in the strong coupling domain. Moreover, the resonances broaden more, for the same decrease in inter-antenna spacing, due to the very strong near-field coupling (Figure 2.4e). This gives a large positive contribution to ΔΦ and ρ. Consequently, a larger ΔΦ and ρ can be obtained in the strong coupling domain.

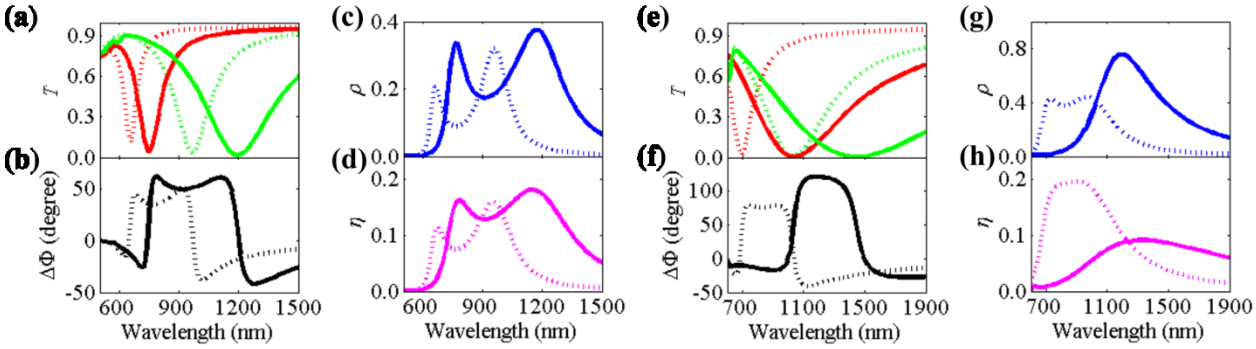

Figure 2.4. **(a)-(d)**: Effect of increasing length in weak coupling domain. T, ΔΦ, ρ and η for L = 140 nm (dotted lines) and L = 180 nm (solid lines). Other array dimensions are w = 40 nm and P = 280 nm. The symmetric resonance redshifts more than the antisymmetric one. This increases spectral spacing between them, and thus broadens ΔΦ and **ρ.** The resonances broaden, and in this case its contribution to increase ΔΦ dominates which increases ρ. **(e)-(h)**: Effect of increasing length in strong coupling domain. T, ΔΦ, ρ and η for L = 150 nm (dotted lines) and L = 190 nm (solid lines). Other array dimensions are w = 40 nm and P = 200 nm. Both eigenmodes redshift more than that in the weak coupling domain for same increase in length. Resonances are much broader. A high ΔΦ and ρ is obtained.

2.3.3 Effect of increasing the antenna's arm width *w*

Increasing the arm width *w* for a fixed arm length *L* makes the L-antenna more like a square, for which the resonances of the eigenmodes would perfectly overlap. Therefore, in either coupling domain, increasing *w* decreases the spectral separation between the resonances as shown in Figure 2.5. The reduced separation between the resonances narrows and increases ΔΦ and ρ. Thus *w* can be used to trade-off between bandwidth and ρ of the device. Moreover, the resonances blueshift in either domain with increasing *w*. This is because the surface currents can deviate more from the arm axis and hence oscillate along shorter paths.

In the weak coupling domain, the antisymmetric resonance blueshifts significantly whereas there is a negligible blueshift in the symmetric resonance. This shows that the antisymmetric resonance condition for 'fat' antennas is not accurately described by models based on the thin-wire approximation [42]. In the strong coupling domain, the stronger near field coupling results in a greater spectral shift and spectral broadening of both eigenmodes for the same increase in arm width, as shown in Figure 2.5(e). A high ΔΦ and ρ are obtained.

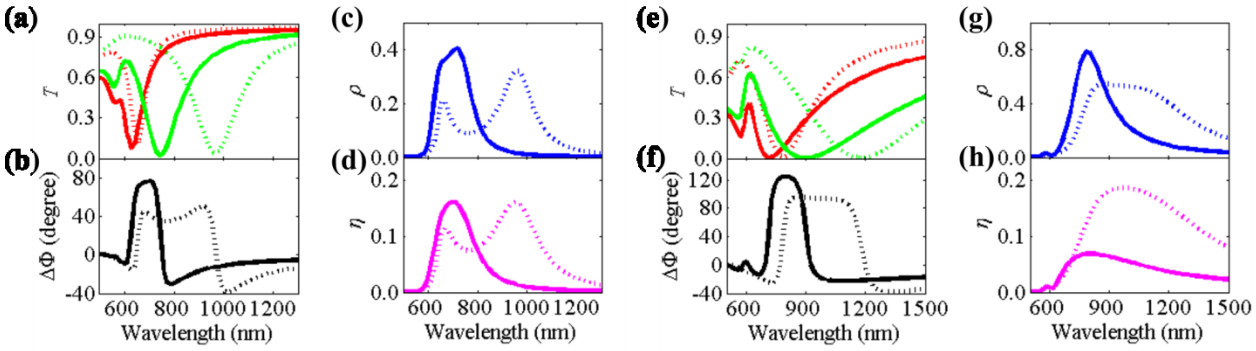

Figure 2.5. (a)-(d): Effect of increasing width in weak coupling domain. *T*, ΔΦ, ρ and η for *w* = 40 nm (dotted lines) and *w* = 80 nm (solid lines). Other array dimensions are *L* = 140 nm and *P* = 280 nm. The symmetric resonance blueshifts negligibly whereas as the antisymmetric resonance blueshifts significantly. This reduces the spectral spacing between them, and thus increases and narrows ΔΦ and ρ. **(e)-(h)**: Effect of increasing width in strong coupling domain. *T*, ΔΦ, ρ and η for *w* = 40 nm (dotted lines) and *w* = 80 nm (solid lines). Other array dimensions are *L* = 170 nm and *P* = 200 nm. Both eigenmodes blueshift and broaden more than that in the weak coupling domain for same increase in width. A high ΔΦ and ρ is obtained.

2.3.4 Effect of increasing the array topology parameter θ

To study different array topologies, we rotate both the source and antenna by angle θ about the z-axis. In the weak coupling domain, the arrangement of the antennas relative to each other, and hence θ, does not have any significant effect. In the strong coupling domain though, we observe that as we increase θ from 45˚, the antisymmetric resonance redshifts and broadens. This is because the arm ends of the neighbouring antennas, which exhibit the strongest field localization for the antisymmetric mode (see Figure 2.1(d)), move closer to one another, thereby strengthening the near-field coupling.

The symmetric resonance, however, does not show a consistent trend. When θ is increased from 45˚, the symmetric resonance redshifts and broadens, but then blueshifts and narrows. This indicates that the overall strength of the near-field coupling for the symmetric eigenmode first increases but then decreases. This behavior can be explained from the fact that while the arm ends of neighbouring antennas move closer to one another with increasing θ, the vortex of each antenna (where the arms meet) which supports the strongest fields for the symmetric resonance (Figure 2.1(c)) moves further from its neighbouring antennas. This can be visualized from Figure 2.2 (b), which shows antennas placed at $\theta = 90$˚.

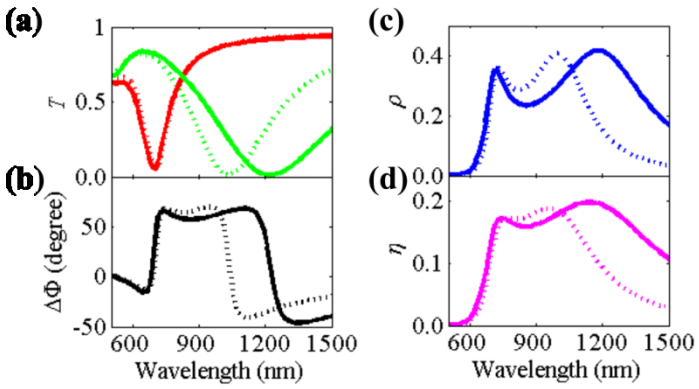

Figure 2.6. **(a-d)** Effect of increasing θ in strong coupling domain. T, $\Delta\Phi$, ρ and η for $\theta = 55$˚ (dotted lines) and $\theta = 75$˚ (solid lines). Other dimensions are $L = 150$ nm, $w = 40$ nm, $P = 200$ nm. Increasing θ redshifts and broadens the antisymmetric resonance. For this specific example the symmetric resonance shows negligible change. The spectral spacing between resonances increases thereby giving a broader $\Delta\Phi$ and ρ.

The topology parameter can thus be tuned such that the antisymmetric resonance redshifts due to stronger coupling while the symmetric resonance undergoes a negligible overall spectral shift, thereby providing a design knob to control the bandwidth. We illustrate a specific example in Figure 2.6 of tuning the array topology to achieve a broader bandwidth.

2.4 Discussion of the efficiency η

Increasing the period P in either domain reduces the fill-factor and hence increases the transmission T (in the overlap region), but reduces the purity ρ as discussed before. Increasing the length L in either domain increases the fill-factor and hence decreases T, but does not always decrease the ρ. Increasing the width w decreases T but increases ρ. Consequently, it is not possible to deduce a general trend of the magnitude of the efficiency η for changing these parameters. However, since changing the topology parameter θ does not change the fill-factor, the magnitude of η follows the same trend as the ρ in the overlap region. Moreover, we do observe that the η profile spectrally shifts in the same direction as ρ for each of the parameters we have discussed here.

2.5 Results and discussion

Based on the effect described above of varying the design parameters, we present a design methodology to design a half-wave plate at a longer wavelength starting from any existing L-antenna array design. Even though the parameter space we explore is limited, the methodology we present only depends on the parameters we study, and therefore can be applied to any existing design. We discuss designing in the weak coupling domain, since it affords larger inter-antenna spacing and hence more tolerance to fabrication inaccuracies.

To shift the eigenmodes, and hence the purity ρ, to a longer wavelength, the arm length L has to be increased. However, this will reduce the inter-antenna spacing. Therefore to increase L without departing from the weak coupling domain, the period P should be increased first. This would maintain the width and spectral range of ρ but reduce its magnitude. Thus P should not be made unnecessarily large. Next, L and arm width w should be scaled up together to redshift and increase ρ. Finally, w can be adjusted to trade-off bandwidth with peak ρ. A larger w will narrow, increase and blue shift ρ. An example of the above recipe is shown in Figure 2.7a.

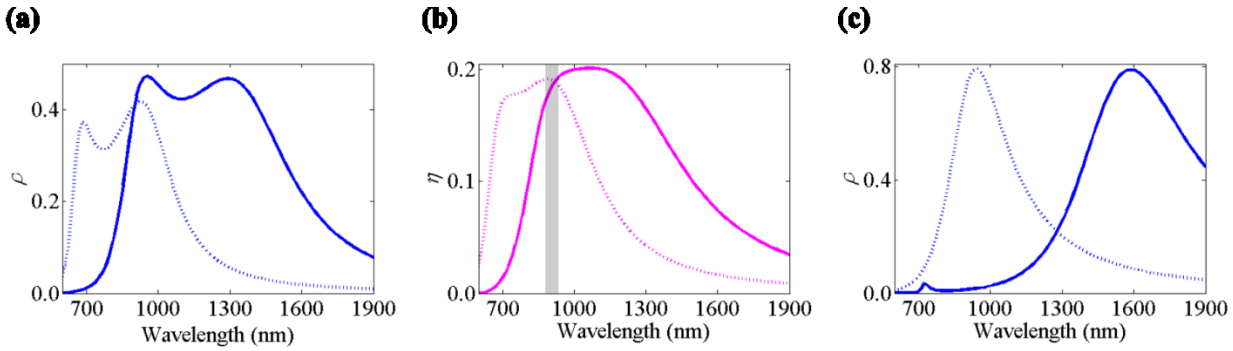

Figure 2.7. **(a)** Illustration of a design methodology to design a half-wave plate at a longer wavelength in the weak coupling domain. The design parameters are: L = 140 nm, w = 40 nm, P = 200 nm (dotted line) and L = 270 nm, w = 80 nm and P = 360 nm (solid lines). **(b)** Illustration of a design methodology to design a half-wave plate to operate at the same wavelength (grey shading) with larger design parameters, for easier fabrication. The design parameters are: L = 140 nm, w = 40 nm, P = 200 nm (dotted line) and L = 260nm, w = 90 nm and P = 360 nm (solid line). Both designs show the same efficiency at 920 nm wavelength (highlighted in grey). **(c)** Illustration of a design methodology to design at longer wavelength in strong coupling domain. ρ is shown for L = 140 nm, w = 40 nm, P = 150 nm (dotted line) and L = 290 nm, w = 60 nm, P = 300 nm (solid line).

The above methodology also affords the possibility of designing an array having larger dimensions, and hence more tolerance to fabrication constraints, but with the same efficiency η at a design wavelength. While the center of the ρ and η profiles redshift using the above methodology, their finite width can enable the final design to give the same η as the initial design at a fixed desired wavelength. An example of this is shown in Figure 2.7b. The final design has much larger antenna dimensions and inter-antenna spacing, but the same efficiency at 920 nm wavelength.

A similar design methodology can be used to design at a longer wavelength in the strong coupling domain. This is viable when sophisticated fabrication processes are available. In applying the design methodology, L needs to be increased to redshift the eigenmodes and ρ. However, to increase L without touching the neighbouring antenna, P should be increased. This will blueshift and reduce ρ. Increasing L would then redshift and increase ρ. Finally, w and θ can be tailored to tradeoff ρ with bandwidth. As mentioned before, a higher ρ is obtained in this

domain as compared to that in the weak coupling domain. An example of this recipe is shown in Figure 2.7c.

2.6 Conclusion

In this work we have provided insights to designing half-wave plates based on the use of L-shaped nanoantenna arrays using the FDTD method. We describe the effect of varying the antenna arm length and width on the half-wave plate performance, and show that the array properties such as the period and array topology provide an important degree of freedom in the design process. We have presented methodologies tailored to available fabrication capabilities, that can be used to design for operation at a desired wavelength while having control over device performance characteristics of purity, efficiency and bandwidth. The results we present here are easily applicable to designing quarter wave plates as well, and can be extended to incorporate other parameters such as antenna thickness. We believe that this work will enable more effective design of ultrathin waveplates with L-shaped nanoantenna arrays.

2.7 Supplementary section

Figure 2.8 shows a screenshot of the Lumerical FDTD simulation file we used for the study presented in this chapter.

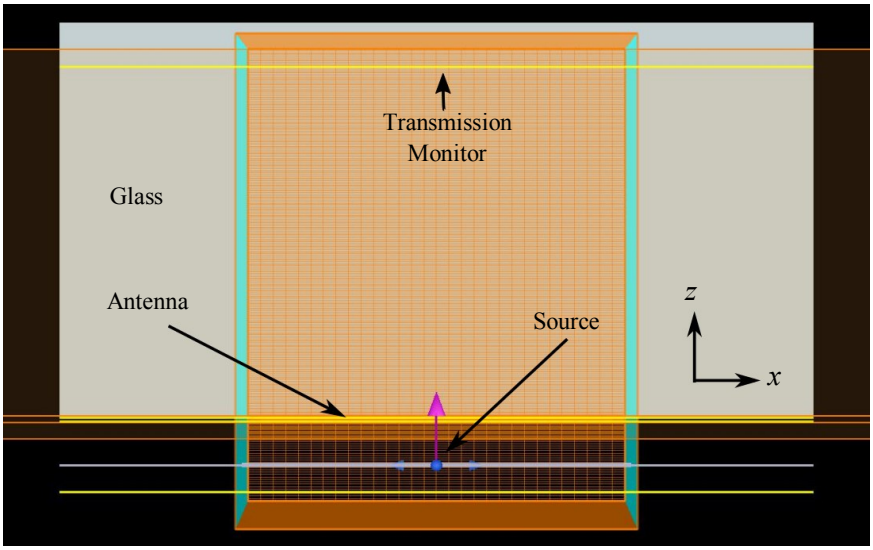

Figure 2.8: Screenshot of our simulation file in Lumerical FDTD.

For each array design, we ran separate simulations for the source polarized along each eigenmode of the antenna. The purpose of this section is to describe the procedure to extract the equivalent response for a right-circularly polarized input from these two simulations, thereby avoiding the need to run an extra simulation for a right-circularly polarized input.

Since we are operating in the regime of linear optics, we can model our array as a system with a response function F, which takes as its input the vector incident field and whose output is the vector field at the transmission monitor. It should be noted that Lumerical FDTD returns field components in the form of complex phasors, and thus so are the fields discussed in the analysis below.

At the source, light is propagating in the positive z direction. We denote light polarized along the symmetric axis, the antisymmetric axis and right circularly polarized light as $|S>$, $|A>$ and $|R>$ respectively, and define them in the Jones vector representation as

$$|S>=\begin{bmatrix}1\\1\end{bmatrix}, \tag{2.4}$$

$$|A>=\begin{bmatrix}1\\-1\end{bmatrix}, \text{and} \tag{2.5}$$

$$|R>=\begin{bmatrix}1\\i\end{bmatrix} \tag{2.6}$$

We are interested in the complex field components E_x and E_y of the response $F(|R>)$, because we can then project these components on left-handed circularly polarized light to calculate the purity ρ and efficiency η. We have dropped the normalization factors because they cancel out in the course of calculating the purity ρ.

From Equation (2.4) - (2.6), $|R>$ can be written in terms of $|S>$ and $|A>$ as

$$|R>=\frac{|S>+|A>}{2}+i\frac{|S>-|A>}{2} \tag{2.7}$$

Since we are in the regime of linear optics, we can treat the antenna array as a linear system. We can thus use Equation (2.4) to decompose $F(|R>)$ as

$$F(|R>) = \frac{F(|S>) + F(|A>)}{2} + i\frac{F(|S>) - F(|A>)}{2} \tag{2.8}$$

Since the linearity of the system holds for each individual field component, we can write Equation (2.8) for each field component as

$$E_x = \frac{E_{xS} + E_{xA}}{2} + i\left(\frac{E_{xS} - E_{xA}}{2}\right), \text{and} \tag{2.9}$$

$$E_y = \frac{E_{yS} + E_{yA}}{2} + i\left(\frac{E_{yS} - E_{yA}}{2}\right), \tag{2.10}$$

where the subscripts S and A refer to the symmetric and antisymmetric polarization. For instance, E_{xS} is the x component of the field at the transmission monitor when the source is linearly polarized along the symmetric axis.

After running separate simulations with the same array design, for the source field polarized along $|S>$ and $|A>$, we can now extract the equivalent response for a $|R>$ polarized input from Equations (2.9) - (2.10). The next step is to project the fields E_x and E_y onto left-handed circularly polarized output.

The projection of the array response, i.e E_x and E_y from Equations (2.9) - (2.10), on left- and right-circularly polarized light is given by

$$|L_{project}> = E_x + iE_y, \text{and} \tag{2.13}$$

$$|R_{project}> = E_x - iE_y \tag{2.14}$$

Since we perform the projection in circularly polarized basis, we calculate the purity ρ by dividing the projection in Equation (2.13) by the total power calculated in circularly polarized basis as

$$\rho = \frac{\left|\left|L_{project}>\right|^2\right.}{\left|\left|L_{project}>\right|^2 + \left|\left|R_{project}>\right|^2\right.} \tag{2.15}$$

We also need to extract the phase of the response to $|S>$ and $|A>$ polarized input in order to extract the phase difference $\Delta\Phi$ reported in previous sections of this chapter. The phase of the response to $|S>$ and $|A>$ input can be extracted as

$$\Phi_S = \text{Angle}\left(E_{xs} + E_{ys}\right), \text{and} \tag{2.16}$$

$$\Phi_A = \text{Angle}\left(E_{xa} - E_{ya}\right) \tag{2.17}$$

The above analysis is valid for the case when the topology parameter θ equals 0. To study the effect of the topology, we rotate both the antenna and the source by the same angle θ about the z-axis. Hence, $|S>$ and $|A>$ now become

$$|\acute{S}>= \begin{bmatrix} \cos\theta + \sin\theta \\ -\sin\theta + \cos\theta \end{bmatrix}, \text{and} \tag{2.18}$$

$$|\acute{A}>= \begin{bmatrix} \cos\theta - \sin\theta \\ -\sin\theta - \cos\theta \end{bmatrix} \tag{2.19}$$

Since the expressions for $|S>$ and $|A>$ change, the decomposition of $|R>$ in terms of $|S>$ and $|A>$ changes as well. After basic arithmetic, we find that $|R>$ can be expressed as

$$|R>= c_1|\acute{S}> + c_2|\acute{A}>, \text{where} \tag{2.20}$$

$$c_1 = \left(\frac{1-i}{2}\right)\sin\theta + \left(\frac{1+i}{2}\right)\cos\theta \text{ and} \tag{2.21}$$

$$c_2 = \left(\frac{1-i}{2}\right)\cos\theta - \left(\frac{1+i}{2}\right)\sin\theta \tag{2.22}$$

By analysis similar to before, we finally obtain

$$E_x = c_1 E_{x\acute{S}} + c_2 E_{x\acute{A}}\,, \tag{2.23}$$

$$E_y = c_1 E_{y\acute{S}} + c_2 E_{y\acute{A}} \tag{2.24}$$

and ρ can be calculated, as before, by using Equations (2.13) - (2.15).

The phase response of $|\acute{S}>$ and $|\acute{A}>$ can be obtained by taking the phase of the projection of the total response, $E_x + E_y$, onto $|\acute{S}>$ and $|\acute{A}>$. In particular,

$$\Phi_{\acute{S}} = \text{Angle}\left(E_x(\cos\theta + \sin\theta) + E_y(-\sin\theta + \cos\theta)\right), \text{and} \tag{2.25}$$

$$\Phi_{\acute{A}} = \text{Angle}\left(E_x(\cos\theta - \sin\theta) + E_y(-\sin\theta - \cos\theta)\right) \tag{2.26}$$

Finally, we note that the phase calculated in Equations (2.25) - (2.26) is the phase response of the antenna combined with the phase of the incident field. To calculate the phase response of just the antenna resonance, similar to the one shown in Figure 2.1e, we subtract the phase of the incident field from the phase response of the system. This is equivalent to normalizing the response of the antenna to the incident field.

As a final comment, we would like to mention a critical feature of Lumerical FDTD, which the author inferred from some tests conducted with the software. At the source, a forward propagating field is described by the phasor convention $e^{-iwt+ikz+i\Phi}$, where k is the wavevector

and Φ is a phase offset. The fields at the source are defined from the perspective of looking *away* from the source. However, at the transmission monitor, the fields are defined while looking *towards* the source.

A consequence of this is that a rotation by θ from the perspective of the source corresponds to a rotation by - θ from the perspective of the monitor. Consequently, θ in Equations (2.25) – (2.26) should be replaced by - θ to extract the correct result from the monitor data.

A second consequence of this change of perspective at the monitor is that a phase offset of Φ in the field is interpreted by Lumerical FDTD as having a phase of - Φ. Hence, the negative of the phase response in Equations (2.16) – (2.17) and Equations (2.25) – (2.26) should be taken for correct results.

Chapter 3

Unconventional response of plasmonic dipole antennas due to an epsilon-near-zero substrate

3.1 Introduction

In the recent past, there has been a considerable interest in materials with near-zero relative permittivity. These are commonly known as epsilon-near-zero (ENZ) materials [49], and they demonstrate very interesting properties such as high efficiency coupling through arbitrary shaped regions, extreme nonlinear responses, deep subwavelength imaging, and phase-mismatch-free nonlinear propagation [50-55]. These ENZ properties can be observed in metamaterials designed to have one or more components of the real permittivity tensor approach zero at a desired wavelength, which we refer to as the ENZ wavelength. They can also be observed at the longitudinal phonon frequency of dielectrics and the bulk plasmon frequency of metals and doped semiconductors.

My research group discovered that a 310 nm thick film of Indium Tin Oxide (ITO) shows an extraordinary optical nonlinearity around its ENZ wavelength. This nonlinearity arises because of a modification of the conduction band free electron population in the ITO in the presence of an intense incident field [55]. This motivated us to explore whether depositing plasmonic dipole antennas on an ITO film backed by a glass substrate, and designed to be resonant near ITO's ENZ wavelength, could further enhance this nonlinearity owing to the field enhancement from the plasmonic resonance. The presence of a glass substrate is necessary to provide support to the ultrathin ITO film. Specifically, we considered a much thinner ITO film, of thickness 23 nm, for applications to ultrathin plasmonic metasurfaces.

Experimental investigation of the linear (low-power) response of the dipole antennas on ITO yielded surprising results. It is well known that dipole antennas show a single optical resonance for incident light polarized along the long axis of the antenna, and that the resonance wavelength is strongly dependent on the dimensions of the antenna. However, our system of dipole antenna arrays showed two resonances whose spectral positions were largely independent of the antenna dimensions. This led us to investigate how the plasmonic antennas interact with

the thin ITO film. In this chapter we thus describe and explain the drastically unconventional behavior of plasmonic dipole antennas when placed on a sub-wavelength ITO layer.

3.2 Our Structure

The structure we investigate in this study consists of different arrays of gold dipole antennas on a 23 nm thick ITO film on top of a glass substrate. The length *L* and width *w* of the antennas is different in each array. Each array has a square lattice with a period *P* of 600 nm, and the antennas are 27 nm thick.

We first consider here three antenna arrays whose dimensions, given as *L* x *w*, are 396 nm x 37 nm, 404 nm x 57 nm and 412 nm x 77 nm. These dimensions were confirmed from scanning electron microscope images, an example of which is shown in Figure 3.1. Figure 3.2 shows the transmission response of these antenna arrays on glass calculated using Lumerical FDTD [45]. The simulations results show, as is well known, that the antennas show a resonance which is symmetric about it center, and whose central wavelength is strongly dependent on the antenna dimensions.

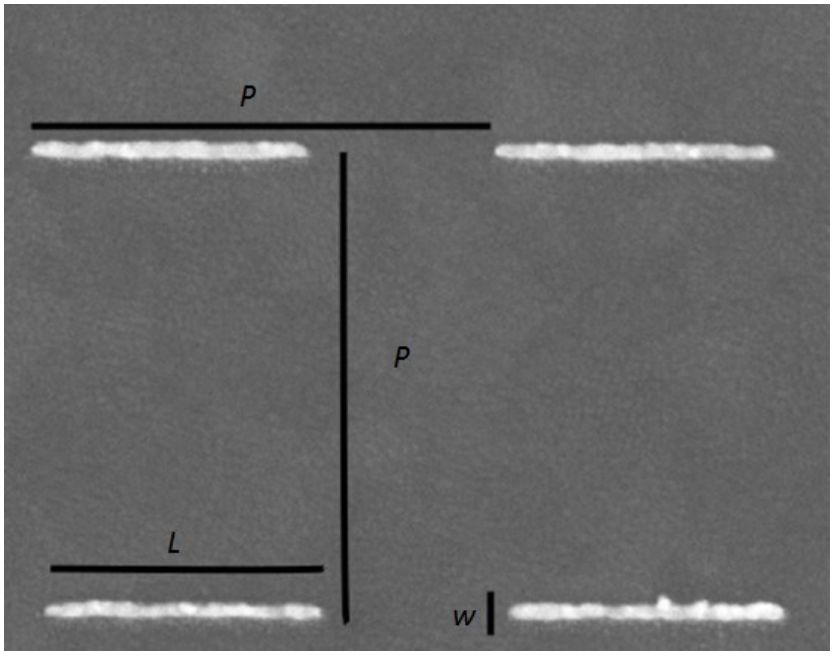

Figure 3.1: Scanning electron microscope image of the fabricated sample. The dipoles have length *L*, width *w* and are arranged in a square array with period *P*.

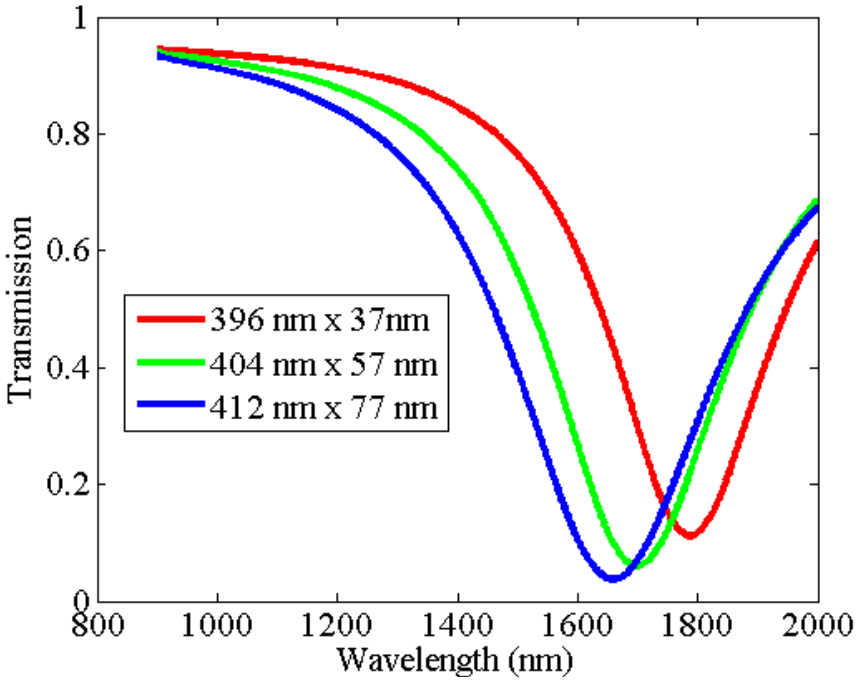

Figure 3.2: Simulated response of dipole antennas on glass substrate. The dimensions of each antenna are shown as *L* x *w*, where *L* and *w* are the arm length and width respectively.

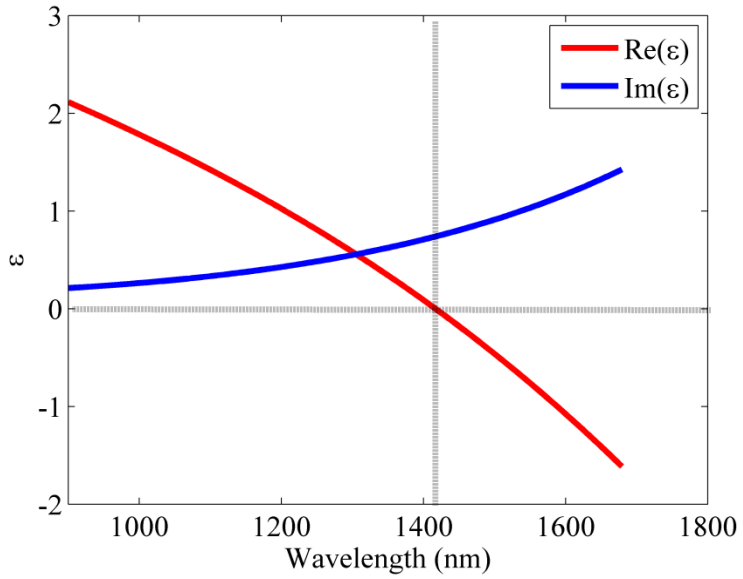

Figure 3.3: Real (red curve) and imaginary (blue curve) permittivity values of our ITO film. The real permittivity becomes zero at wavelength of 1417 nm, as indicated in the figure by grey lines.

The ITO film-on-glass samples were obtained from a commercial supplier. Since ITO is a non-stoichiometric material, its material properties depend on the growth and deposition conditions. The permittivity, ε, values of our ITO sample were obtained from ellipsometry measurements and are shown in Figure 3.3. We observe that the real part of the permittivity goes through zero at wavelength 1417 nm, henceforth referred to as λ_{ENZ} .

Figure 3.4 shows the dispersion curve of the 23 nm ITO layer, plotted with respect to the normalized longitudinal (parallel to the film surface) component of the k-vector, $k_{\|}$. The dispersion curve was obtained by computing the local minima of the ITO film's reflectance spectrum using the Nelder Mead method. This measurement and calculation was performed by a co-author of this project. We see that around λ_{ENZ}, a mode with a very flat dispersion profile, and hence a very high density of states, is supported by the ITO film. We call this the epsilon-near-zero (ENZ) mode of our ITO film.

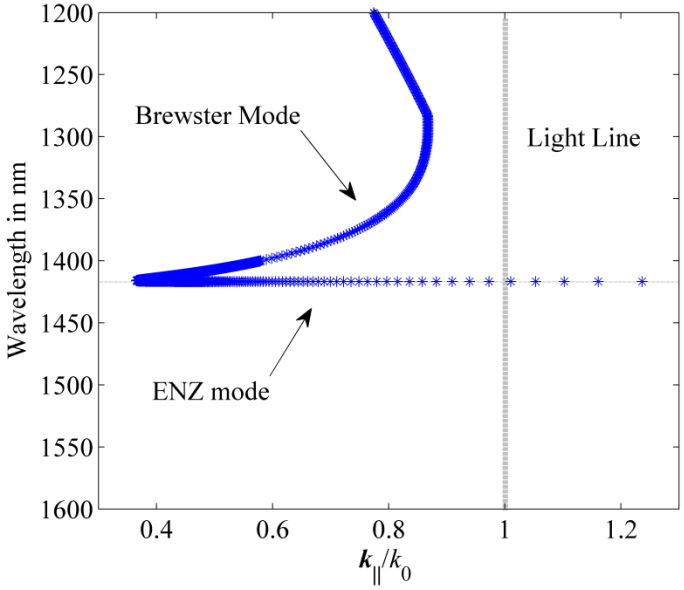

Figure 3.4: The dispersion curve of the ITO film showing the Brewster mode and the epsilon-near-zero (ENZ) mode. The parallel wavevector $k_{\|}$ is shown in $1/k_0$, where k0 is the free space k-vector. This figure is reproduced here with the permission of M. Z. Alam[2].

In addition to the ENZ mode, we also see another mode around the ENZ wavelength which does not have a flat profile. This is known as the Brewster mode which occurs in thin plasmonic films around the plasma frequency [56]. It should be mentioned here that modes with

a dispersion similar to the ENZ mode and Brewster mode shown above have been studied previously in thin dielectric films [57], metallic films [58] and semiconductor films [59]. The part of the ENZ mode below the light line has been referred to as the Ferrel-Berreman mode by Vassant et al [57].

For purposes of this chapter and the next, we are primarily interested in the ENZ mode. We therefore describe its specifics in detail here. ENZ modes arise in ultrathin conductive films near the plasma frequency, or in ultrathin dielectric films near the longitudinal phonon frequency. This mode supports an enhancement of the transverse (perpendicular to the film surface) field component in the thin ENZ film, whose intensity increases with decreasing film thickness [58]. ENZ films and have thus been suggested for use as ultrathin absorbers [57].

The field enhancement of the transverse component in the film can be intuitively understood through the argument presented by Vassant et al [57]. Since the transverse component of the displacement vector has to be continuous across the interface between the film and the surrounding medium, the field in the film is given by

$$E_{z,\text{film}} = \frac{\varepsilon_{\text{film}}}{\varepsilon_{\text{medium}}} E_{z,\text{medium}}, \tag{3.1}$$

where z refers to the transverse direction and the subscript 'medium' refers to the surrounding medium. It can be seen form Equation (3.1) that as the permittivity $\varepsilon_{\text{film}}$ of the film approaches zero, the field $E_{z,\text{film}}$ in the film enhances. Moreover, since the mode is formed in ultrathin films of thickness less than the skin depth, the field intensity is uniform along the transverse direction in the film [57, 58].

We would like to conclude the discussion of the ENZ mode by emphasizing that this mode occurs only in ultrathin films. As such, the nonlinearity observed in the 310 nm thick ITO film around its ENZ wavelength does not arise due to the ENZ mode.

3.3 Experiment and Results

Light from a tungsten halogen source, polarized along the long axis of the antenna, was used to excite the sample. The transmitted light was measured with an optical spectrum analyzer, and this transmission was normalized to transmission through the bare ITO film on glass. A schematic of the experimental set-up is shown in Figure 3.5. A flip mirror, mounted before the objective lens, was used to route light to a lens and camera in order to image the antenna arrays in the sample. This imaging system is not shown in the schematic above. The results of the experiment are shown in Figure 3.6.

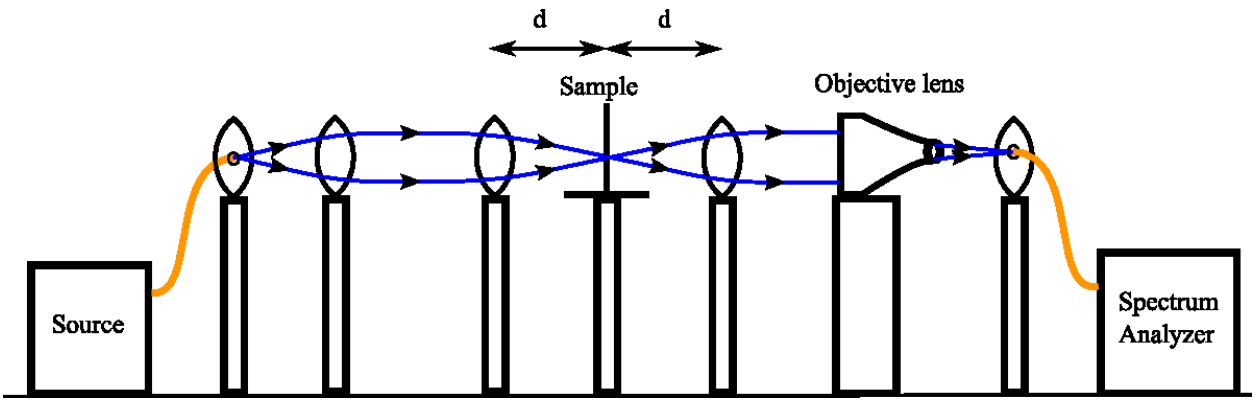

Figure 3.5: Schematic of the experimental set-up used to characterize the linear optical response of the antenna array on ITO substrate.

We observe a surprising response which is markedly different from the simulated response of the antenna-on-glass system. Firstly, the transmission shows two resonance dips as opposed to one. Secondly, both resonances show a negligible spectral shift with the varying antenna dimensions. The only difference is in the strength of the extinction. Due to the limitation of the operating range of our spectrum analyzer, we could not fully measure the second, longer wavelength resonance. However, FDTD simulation results for the antenna-on-ITO structure, as shown in Figure 3.6, confirm that spectral positions of both dips in transmission are largely independent of the antenna dimensions. The dispersion of the ITO in the simulations was

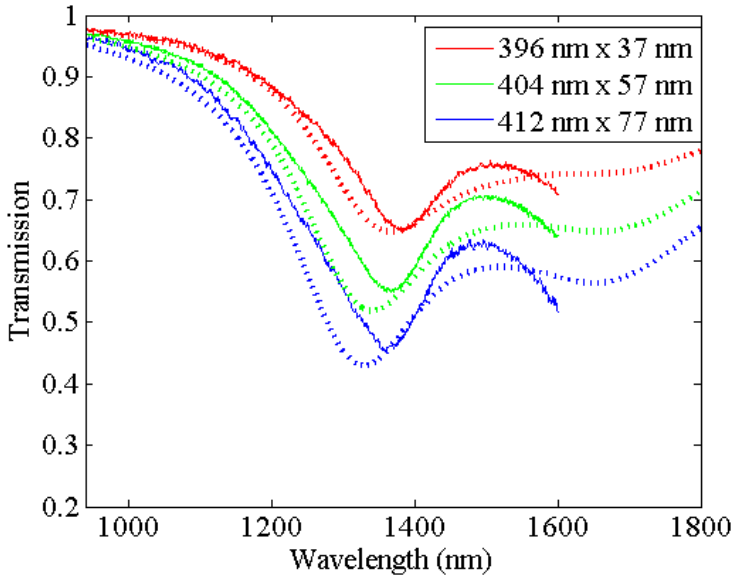

Figure 3.6: Measured (solid curves) and simulated (dotted curves) of transmission of antenna arrays on ITO substrate. The transmission is normalized to the transmission through the bare ITO. The dimensions of each antenna are shown as L x w, where L and w are the arm length and width respectively.

modelled using the measured permittivity data shown in Figure 3.3. Mesh convergence for the simulations was achieved for a mesh step of 2 nm in each dimension for the span of the antenna and ITO. For consistency with experiment, the simulated transmission was normalized to the simulated response of the bare ITO film.

We also performed measurements on a number of other antenna arrays with different dimensions and observed the same features as described above. The results of these measurements are shown in Figure 3.7a, and the corresponding simulated response of antenna on glass is illustrated in Figure 3.7b.

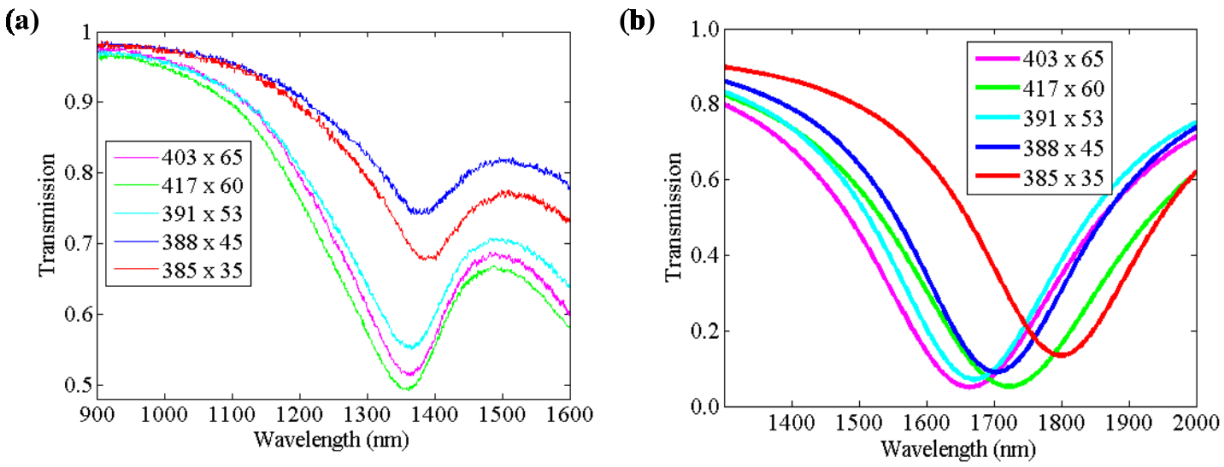

Figure 3.7: (a) Measured transmission response of additional antenna arrays on ITO substrate. The transmission is normalized to the transmission through the bare ITO film. The dimensions of each antenna are shown as L x w, where L and w are the arm length and width respectively. **(b)** Simulated response of antenna arrays on a glass substrate, corresponding to the antennas in **(a)**.

3.4 Discussion

We interpret the two dips in transmission around λ_{ENZ} as split resonances due to coupling between the antenna resonance and the ENZ mode of ITO. The viability of this interpretation is strengthened by the fact that the ENZ modes have a very high density of states. This makes coupling to these modes very likely. Moreover, simulations of an antenna array with dimensions of length $L = 404$ nm, width $w = 57$ nm and period $P = 600$ nm, show that the spectral positions of the two resonances of the antenna-on-ITO system show very little dependence on the longitudinal (parallel to the film surface) component of the k-vector, $k_{\|}$. The simulation results, shown in Figure 3.8, indicate that two resonance features occur at wavelengths 1350 nm and 1680 nm which exhibit very little dependence on $k_{\|}$. Such a behavior is expected from coupling between the antenna and the ENZ mode, since they both have resonances which do not depend on the k-vector. It is also important to note that the period of each array is large enough such that there is no near-field coupling between the antennas. This is

confirmed from the simulation results for transmission of antennas on glass, such as in Figure 3.2. Therefore, the split resonances we observe cannot be attributed to inter-antenna coupling.

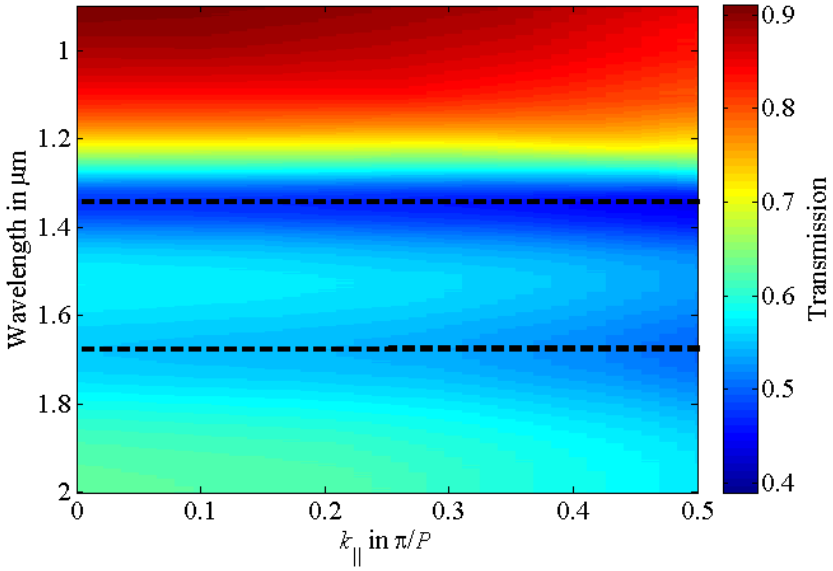

Figure 3.8: The simulated transmission response of the antenna-on-ito system as a function of wavelength and longitudinal component of the wave-vector, $k_{||}$. The dimensions of the antenna array L = 404 nm, w = 57 nm and P = 600 nm. Two resonances are observed around wavelengths 1350 nm and 1700 nm. Both resonances show very little dependence on the k-vector. This figure is reproduced here with the permission of S. A. Schulz[1].

To visualize in a more lucid manner that a splitting of resonances is indeed occurring due to coupling of the antenna resonance to the ENZ mode, we run simulations in which we vary just the antenna width w, from 170 nm to 50 nm, for a fixed length L = 360 nm. We choose the antenna dimensions such that the antenna resonance on glass spans across λ_{ENZ}, as shown in Figure 3.9, which enables us to better understand the interaction between the arrays and the ITO film. As expected, the resonance of the antennas on glass blueshifts with increasing width.

The transmission response of the antennas on ITO is shown in Figure 3.10. The antenna width is varied in steps of 10 nm from w = 50 nm to w = 170 nm. The results clearly show that a resonance splitting occurs around λ_{ENZ}, and the split resonances do not show a significant spectral shift with varying antenna size. The dashed line in Figure 3.10 indicates λ_{ENZ}. As before, the transmission response is normalized to the transmission though the bare ITO film.

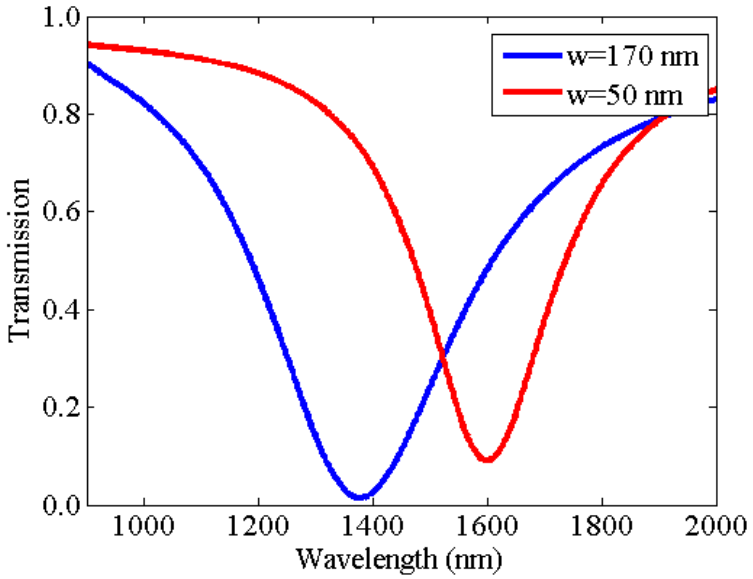

Figure 3.9: Simulated response of antennas on glass for fixed arm length L = 360 nm. The figure shows that by varying the arm width from w = 50 nm to w = 170 nm, the antenna's resonance on glass sweeps the ENZ wavelength.

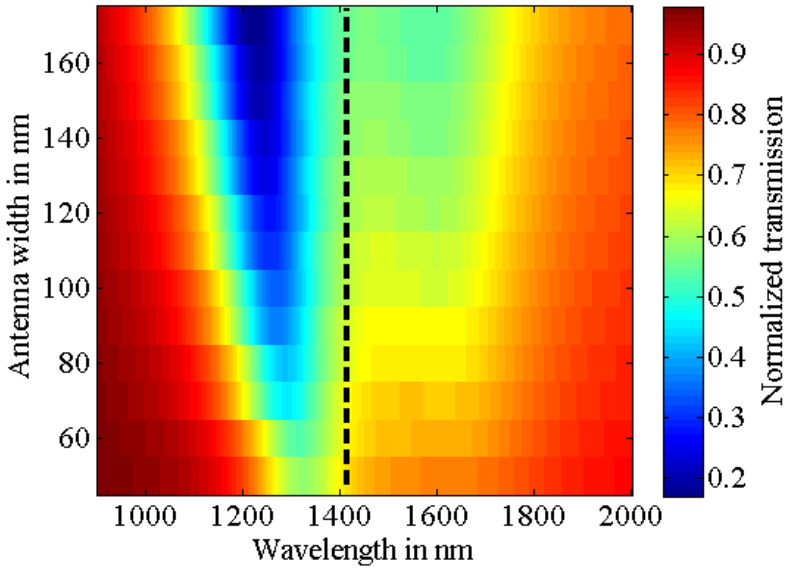

Figure 3.10: Transmission response of the dipole antennas on ITO for varying width and fixed length L = 360 nm. The transmission is normalized to the transmission through the bare ITO film. A splitting of resonances is observed around the ENZ wavelength, indicating coupling of the antenna resonance to the ENZ mode. The ENZ wavelength is shown by the dashed vertical line.

To further consolidate our view, we used Lumerical FDTD to calculate the distribution of the field intensity in the antenna-on-ITO system, for an antenna of dimensions L = 412 nm and w = 77 nm. The corners of the antenna in the simulation have a radius of curvature of 20 nm. The results are shown in Figure 3.11. We show the field component perpendicular (transverse) to the film surface since, as mentioned before, ENZ modes are characterized by unique features of their transverse component. In our FDTD simulation file, the transverse direction is along the z-axis.

For a comprehensive understanding of the interaction between the antenna and the ITO substrate, we calculate the fields at three different wavelengths, λ, which correspond to three distinct wavelength regions.

(i) $\lambda = 1.00$ μm, which is in the wavelength region far from both the antenna resonance and λ_{ENZ} where the ENZ mode is supported.

(ii) $\lambda = 1.33$ μm, which in the wavelength region close to λ_{ENZ} but far from the antenna resonance

(iii) $\lambda = 1.66$ μm, which is far from λ_{ENZ} but close to antenna resonance.

In the first region (λ=1.00 μm), light does not interact with the antenna nor the ITO.

Hence we observe a modest intensity enhancement (Figure 3.11a), and correspondingly a high transmission (Figure 3.5).

In the second region ($\lambda = 1.33$ μm), light interacts more with the antenna and we are also close to the ENZ wavelength. The first, shorter wavelength resonance of the combined system is observed around this wavelength (Figure 3.5). The field distribution in the ITO (Figure 3.11b) shows a hallmark feature of ENZ modes, i.e, a high intensity field uniform in the transverse (z) direction which ends abruptly at the edge of the film [57]. An exception to this behavior is observed at the ITO-antenna interface because of the field enhancement around the antenna. The field distribution in the system thus shows features of both the antenna resonance and the ENZ mode.

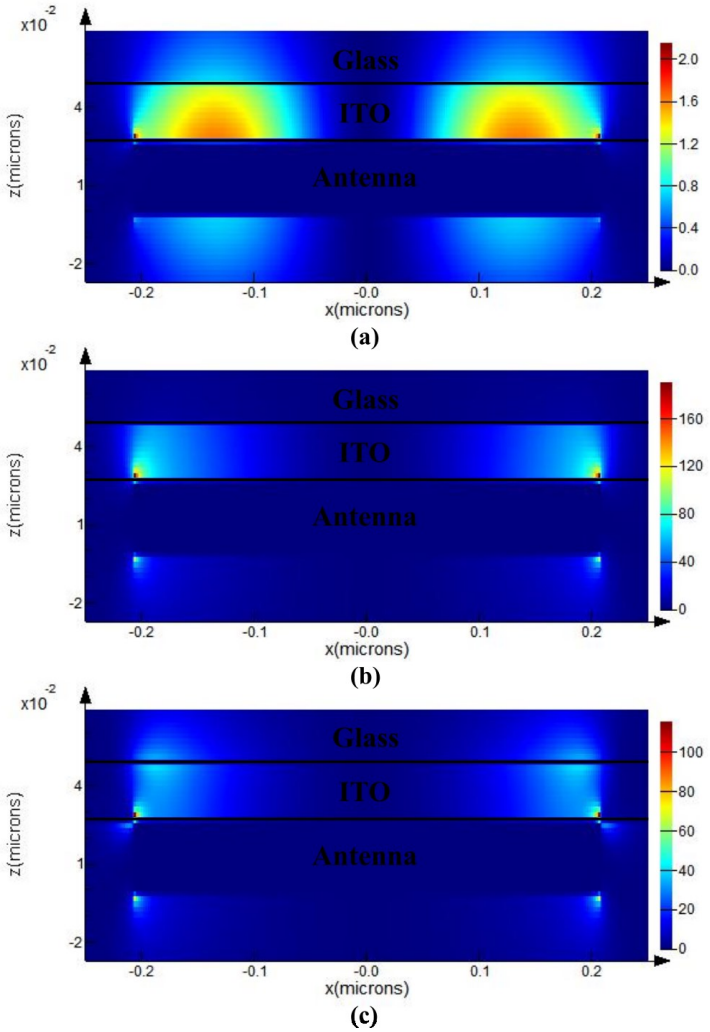

Figure 3.11: Intensity distribution of the transverse (z) component of the field in the antenna-on-ito system at different wavelengths λ. The intensity is normalized to the intensity of the incident field. Dimensions of antenna considered are L = 412 nm and w = 77 nm. Field distribution for λ = 1.00 μm. The light weakly interacts with both the antenna and the ENZ mode and hence negligible field enhancement is observed. **(b)** Field distribution for λ=1.33 μm**,** which shows characteristics of the ENZ mode in the ITO film. **(c)** Field distribution for λ =1.66μm. Some characteristics of the ENZ mode are seen.

As we move to an even higher wavelength ($\lambda = 1.66$ μm), we are further from the ENZ wavelength and closer to the antenna resonance. The second, longer-wavelength resonance of the combined system is observed near this wavelength (Figure 3.5). As shown in Figure 3.11c, the field distribution in the ITO film shows some features of the ENZ mode, i.e a strong field enhancement and a somewhat uniform z-dependence. The antenna also exhibits a strong field

enhancement. Therefore, the intensity distribution at the second resonance also shows features of both the antenna resonance and the ENZ mode. This indicates that the dual resonances of the system resonance are arising from the coupling of the antenna resonance to the ENZ mode.

Additionally, at $\lambda = 1.66$ μm, we do observe a field enhancement in regions on the ITO-glass interface. This can be explained from the fact that ITO has a negative permittivity beyond its λ_{ENZ}. Hence it can support a SPP mode on the ITO-glass interface. We thus attribute the field enhancement at the ITO-glass interface to this SPP mode.

It is important to note that part of the ENZ mode above the light line, which is a bound mode, is not excited under normal incidence in bare ITO films. Hence a confined, enhanced field is not observed in a bare ITO film under normal incidence. We have confirmed this with simulations. However, in the antenna-on-ITO system, scattering by the plasmonic antennas provides the necessary momentum matching to excite the part of the ENZ mode above the light line even under normal incidence. This therefore enables to obtain a confined, high intensity field in the ITO film as shown in Figure 3.11.

For pedagogical purposes, we note that the field enhancement at the antenna-ITO interface for $\lambda = 1.66$ μm cannot be due to the excitation of a SPP mode. This is because both the antenna and ITO have negative values of permittivity in this wavelength region, which would not satisfy the SPP mode condition given by Equation (1.5). Similarly, we do not see a SPP mode at the ITO-glass interface at $\lambda = 1.33$ μm, since both the ITO and glass have positive values of permittivity at this wavelength.

3.5 Conclusion

We have shown that properties of plasmonic dipole antennas can be drastically modified by the presence of a thin film ENZ substrate. We have provided evidence that the unconventional response arises because of coupling between the antenna resonance and the ENZ mode of the ITO film. We believe our findings would pave the way for very exciting applications, such as to further enhance the already strong optical nonlinearity of ITO by utilizing the strong field enhancements provided by the ENZ mode.

Chapter 4

Enhancing the nonlinearity of indium tin oxide using plasmonic nanoantennas

4.1 Introduction

One of the key objectives in the field of nonlinear optics is to have materials whose refractive index can be altered significantly by low power radiation. Our research group discovered that a thin indium tin oxide (ITO) film, of thickness 310 nm, demonstrates an exceptionally large intensity-dependent refractive index around the region where the real part of its permittivity vanishes [55].This motivated us to use plasmonic dipole antennas, of 27 nm thickness, on a 23 nm ITO substrate to further enhance the strong nonlinear optical response of ITO. We consider a thinner ITO film with an aim to demonstrate how the presence of plasmonic dipole antennas can induce huge nonlinearity in ultrathin ITO films.

In chapter 3, we discussed the intriguing linear optical response of plasmonic dipole antennas on a thin ITO substrate. We observed a split resonance around the epsilon-near-zero (ENZ) wavelength, λ_{ENZ}, of the ITO. In this chapter, we discuss the results of a study conducted on the nonlinear response of this antenna-on-ITO structure. Specifically, we discuss the intensity-dependent refractive index of the structure. This study is under progress at the time of this writing.

The refractive index n of a nonlinear medium as a function of the time-averaged incident intensity I is given by [60]

$$n = n_0 + n_2 I \,, \tag{4.1}$$

where n_0 is the linear refractive index and n_2 is the intensity-dependent refractive index. A positive n_2 leads to self-focusing by the medium, whereas a negative n_2 leads to self-defocusing.

For materials exhibiting two-photon absorption, the absorption coefficient of the material is given by [60]

$$\alpha = \alpha_0 + \beta I \,, \tag{4.2}$$

where α_0 is the linear absorption coefficient and β is the two-photon absorption coefficient. A positive β corresponds to two-photon absorption, whereas a negative β denotes saturable absorption [60]. For our particular structure consisting of antennas on ITO, two-photon absorption does not occur in the wavelength region of our interest. A negative β in this case is attributed to reverse saturable absorption [61].

The intensity I of the beam in the medium is given as

$$I(s) = I_0 e^{-\alpha s} \,, \tag{4.3}$$

where I_0 is the peak intensity in the medium and s is the length the beam propagates in the medium. The intensity-dependent refractive index n_2 induces an intensity-dependent phase in the beam passing through the medium. We denote this phase by Φ_{n_2}, which is given by [60]

$$\Phi_{n_2} = n_2 k_0 I_0 L_{(\text{eff})} \,, \tag{4.4}$$

where k_0 is the free-space wavevector. $L_{(\text{eff})}$ is the effective interaction length of the medium and is given by

$$L_{(\text{eff})} = \frac{1 - e^{-\alpha L}}{\alpha} \,, \tag{4.5}$$

where L is the physical length of the medium. For the case where $\ll 1$, $L_{(\text{eff})} \to L$. This condition was satisfied for our ultrathin antenna-on-ITO sample. Therefore, if we model the complete antenna-on-ITO structure as a nonlinear medium with effective intensity-dependent index $n_{2(\text{eff})}$, then the intensity-dependent phase induced by the structure will be

$$\Phi_{n_2} = n_{2(\text{eff})} k_0 I_0 L \tag{4.6}$$

The loss incurred by a beam propagating through a medium appears as an imaginary phase shift induced in the beam, which can be expressed in terms of the imaginary (linear) refractive index, n'', of the medium. The absorption coefficient α is related to the imaginary refractive index by:

$$\alpha = 2k_0 n'' \tag{4.7}$$

Analogously, the intensity-dependent absorption coefficient, βI, of a beam in a nonlinear medium can be expressed in terms of the imaginary component n_2'' of the intensity-dependent refractive index as

$$\beta I = 2k_0 n_2'' I\,, \tag{4.8}$$

which yields

$$\beta = 2k_0 n_2'' \tag{4.9}$$

We can thus define the intensity-dependent imaginary phase, Φ_β, induced in the beam by the antenna-on-ITO structure in terms of the latter's effective two-photon absorption coefficient, $\beta_{(\mathrm{eff})}$, as

$$\Phi_\beta = \frac{1}{2}\beta_{(\mathrm{eff})} I_0 L \tag{4.10}$$

In the following, we describe an experimental method to determine the intensity-dependent phase shifts in our sample, which can then be used to extract values of $n_{2(\mathrm{eff})}$ and $\beta_{(\mathrm{eff})}$ of our sample using the relations described above. The sample consists of square antenna arrays of period P = 600 nm, with the antenna having dimensions of length L = 370 nm and width w = 120 nm. The antenna is designed to be resonant at the ENZ wavelength λ_{ENZ}. Figure 4.1 shows the measured linear optical response of the sample. The transmission is normalized to the

transmission through the bare ITO film. The response of the sample shows characteristics similar to those discussed in the preceding chapter. Specifically, we observe split resonances at wavelengths 1286 nm and 1623 nm.

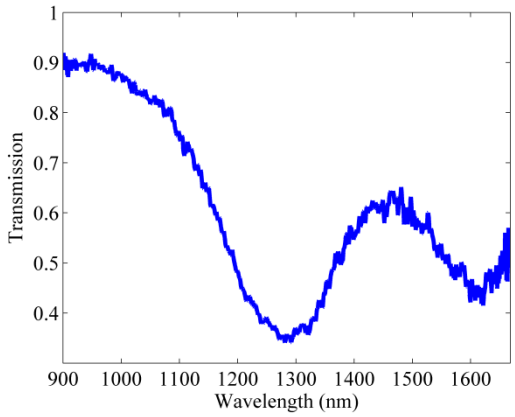

Figure 4.1: Measured linear optical response of an antenna array with dimensions of length L = 370 nm, width w = 120 nm and period P = 600 nm. The transmission is normalized to the transmission through the bare ITO film.

4.2 Methods

We use the z-scan method [62] to determine the intensity-dependent refractive index of our antenna-on-ITO structure. A schematic of the experimental set-up is shown in Figure 4.2. We first describe the experimental set-up, followed by a discussion of how this method can be used to characterize the intensity-dependent refractive index.

Pulsed light from an optical parametric amplifier (OPA) is passed through a half-wave plate and a polarizing beam splitter (PBS) to control the incident power illuminating the sample. The PBS transmits light polarized along the long-axis of the dipole antenna. A pinhole (PH1) of diameter 0.3 mm is used to select a nearly top-hat beam profile, which diffracts in the far field to give an Airy beam profile. A second pinhole (PH2) truncates the Airy beam at its nulls, thereby transmitting a 'trimmed Airy beam'. This beam is then collimated with lenses L1 and L2.

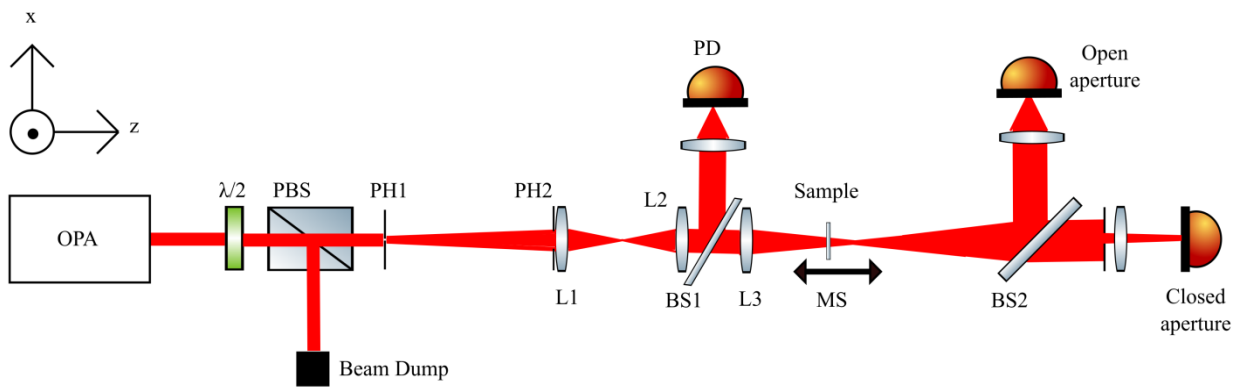

Figure 4.2: The experimental set-up we use to characterize $n_{2(\text{eff})}$ and $\beta_{(\text{eff})}$. Pulsed light from an optical parametric amplifier (OPA) is passed through a half-wave plate, a polarizing beam splitter (PBS) and pinholes (PH1 and PH2). It is then collimated using lenses L1 and L2. The average input power is detected before the sample using a beam-splitter (BS1) and a photodetector (PD1). The z position of the sample is adjusted using a motorized stage (MS). Light is focused on the sample using the lens L3. Light transmitted through the sample is then passed through a beamsplitter (BS2) and routed to the closed aperture and open aperture photodetectors. This figure has been reproduced with the permission of M. Zahirul Alam[2].

The average input power is detected before the sample using a beam-splitter (BS1), whose transmission is wavelength dependent, and a photodetector (PD1). This power value is controlled by adjusting the half-wave plate in the beginning of the set-up. A focusing lens (L3), of focal length f = 100 mm, is then used to excite the sample. The null-to-null beam diameter before the focusing lens is 7.5 mm. The sample is mounted on a motorized stage (MS) whose position is varied in the z direction. Light transmitted from the sample is then passed through a beam-splitter (BS2) and routed to:

(i) a *closed aperture*, i.e a pinhole, followed by a photodetector. The average power measured here, as a function of the sample position z, is referred to as the closed aperture signal.

(ii) directly to a photodetector. The average power measured here, as a function of z, is referred to as the open aperture signal. This name signifies that no aperture is present before the photodetector.

We now describe how the above set-up, which is an implementation of the z-scan method, can be used to characterize the intensity-dependent refractive index n_2 and the two-

photon absorption coefficient β of a nonlinear medium. In essence, the set-up measures the transmitted power in the far field of the nonlinear medium sample as a function of its position z. Typically, the focal plane is chosen to be the reference position, i.e $z = 0$. The technique is thus appropriately named as the z-scan method [62]. The closed aperture is aligned with the center of the beam profile, and its transmission is therefore sensitive to changes in the wavefront curvature at the center of the beam.

Changes in the beam wavefront are related to the nonlinear refractive index n_2 for the following reason. As the sample is scanned in the z direction, the spot size and hence the peak intensity of the illuminating beam changes. Consequently, the phase shift, Φ_{n2}, induced in the beam due to the intensity-dependent refractive index n_2, changes. This in turn alters the wavefront curvature at the closed aperture.

For the case where the sample is much thinner than the diffraction length of the focused beam, the sample can be regarded as a thin lens of variable focal length. Under this condition, which does apply to our particular case, we can intuitively understand the response of the closed aperture signal as a function of z.

For a negative value of nonlinear index n_2, the sample behaves as a diverging lens. Far from the focus, the nonlinear effects are negligible and no change is observed in the power

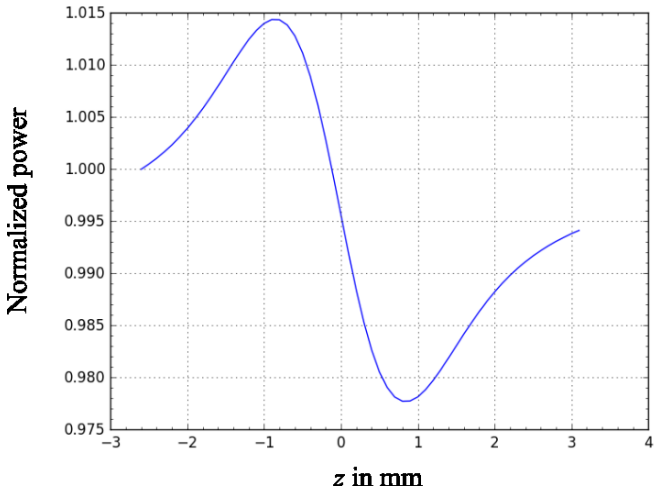

Figure 4.3: Simulated close aperture signal for a medium with a negative value of n_2.

transmitted through the closed aperture. We take this power to be our reference, to which we normalize the closed aperture signal. As the sample moves towards the focus, the beam transmitted through the sample tends to collimate. This results in an increase in the transmitted power through the closed aperture. As the sample moves beyond the focal plane, it tends to diverge the beam which decreases the closed aperture signal. This indicates that there is a null in the change in transmitted power as the sample crosses the focal plane.

The above discussion leads to the conclusion that a prefocal maximum and a postfocal minimum in the closed aperture signal is an indication of a negative n_2. A positive n_2, by a similar argument, would result in a prefocal minimum and a postfocal maximum in the closed aperture signal. An example of a closed aperture signal for a medium with negative n_2 is shown in Figure 4.3.

The closed aperture signal can be described mathematically using different theoretical approaches [61 – 62]. The mathematical expressions incorporate the real and imaginary nonlinear phase shifts, i.e Φ_{n2} and Φ_{β}, respectively. In the absence of nonlinear absorption, there is no contribution to the closed aperture signal from Φ_{β}. Therefore, Φ_{n2} can be extracted by fitting theoretical models to just the closed aperture data. However, in the case of a medium having intensity-dependent absorption, the transmission through the closed aperture is effected by both the real and imaginary phase shifts. Therefore, in this case it is not possible to accurately extract Φ_{n2} from the closed aperture signal alone.

The open aperture signal, on the other hand, is sensitive to the imaginary part of the nonlinear phase shift, Φ_{β}, but not to Φ_{n_2}. This is because the open aperture signal measures power in the entire beam profile and hence is insensitive to changes in the wavefront curvature. Intuitively, the open aperture signal would give a peak (for negative β) or valley (for positive β) as the sample crosses the focus, where the intensity is maximum and thus where the nonlinear contribution βI to the absorption coefficient is also maximum. As an example, Figure 4.4 shows an open aperture signal for a positive value of β.

Experimental open aperture signals, however, do not look like Figure 4.4. To elucidate on this, consider Figure 4.5(a) which shows an open aperture signal measured by the author. The zero point on the horizontal axis is arbitrary.

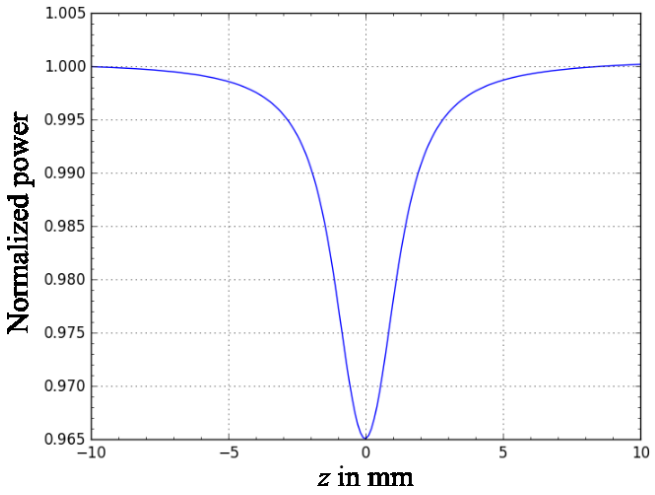

Figure 4.4: Simulated open aperture signal for a medium with a positive value of β.

We notice that the power in the beam, transmitted thorugh the sample, changes over a large range in z. This is because beyond the Rayleigh range, the beam spills over the size of the sample. This introduces a change in transmission through the sample due to a change in linear absorption. The contribution of the nonlinear absorption to the open aperture signal can be found within the Rayleigh range, where the linear transmission response tends to flatten out. This is shown as the grey region in Figure 4.5(a). Within this region, the portion of the beam interacting with the sample is constant, and hence any change in absorption is due to nonlinear optical effects.

In order to isolate the nonlinear absorption response similar to the one in Figure 4.4, we take the reference transmission at z = 8.9 mm. This choice of the reference point, indicated by a red cross in Figure 4.5(a), is chosen arbitrarily but lies in the region where the linear transmission response is flat. The open aperture signal is normalized to this reference, and only the part of the signal where the linear transmission is flat (shaded grey in Figure 4.5(a)) is kept. Applying this procedure to the data shown in Figure 4.5(a) yields an open aperture signal shown in Figure 4.5(b), which can then be used to extract the value of Φ_β and hence $\beta_{(\text{eff})}$.

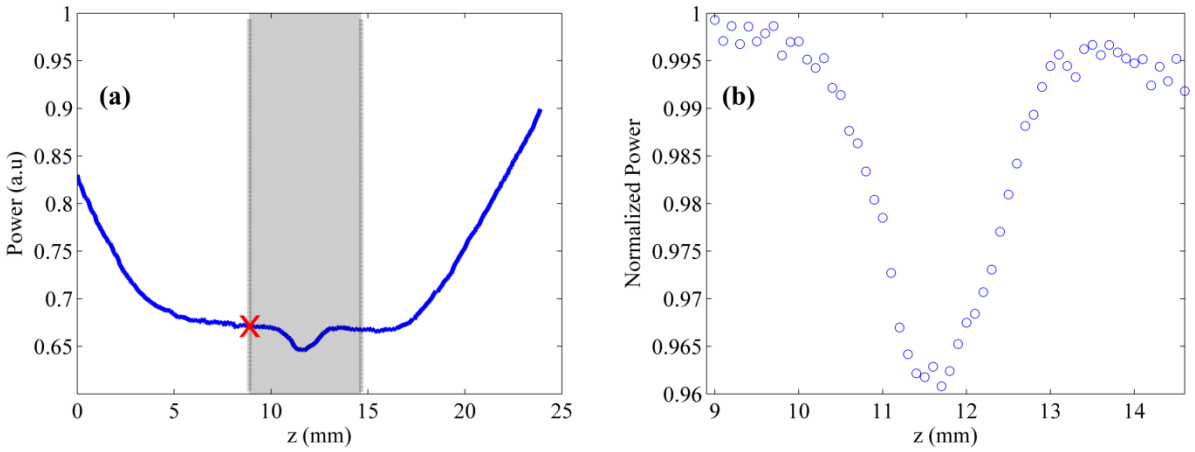

Figure 4.5: (a) Experimentally measured raw data of the open aperture z-scan signal for 1380 nm wavelength. Beyond the Rayleigh range, i.e, $z < 8.9$ mm and $z > 14.6$ mm (shaded grey), the transmission changes due to the beam spilling over the sample. The red cross gives an example of a good choice of the reference transmission. **(b)** Open aperture signal obtained after normalizing the data in **(a)** to a properly selected reference transmission, and keeping only the data points where the beam stays within the sample. The curve in **(b)** can be used to extract Φ_β.

Mathematical expressions can be derived for the open aperture signal, and hence Φ_β can be extracted from the open aperture signal through curve fitting. The value of Φ_β can then be fed in expressions for the closed aperture signal to extract Φ_{n2}. Finally, n_2 and β can be calculated from the phase shifts using Equations (4.6) and (4.10).

For our particular experiment, we know the average power, P_{avg}, of the beam illuminating the sample. The beam consists of pulses, each with duration τ = 150 fs, which have a repetition rate of f_{rep} = 1 kHz. The peak power, P_{peak} of the beam is obtained as

$$P_{\text{peak}} \approx \frac{P_{\text{avg}}}{\tau f_{\text{rep}}} \tag{4.11}$$

We would like to calculate the peak intensity of the beam at the focus, and then use it in Equations (4.6) and (4.10) to calculate $n_{2(\text{eff})}$ and $\beta_{(\text{eff})}$. The peak intensity can be obtained using the peak power P_{peak} and spot size of the beam at the focus. We simplify the problem of

calculating the spot size by treating the trimmed Airy beam as a Gaussian. This is a reasonable approximation because the trimmed Airy beam and the Gaussian beam have similar profiles.

The null-to-null beam diameter of the Airy beam illuminating the focusing lens, L3, is 7.5 mm. A circular Gaussian beam has 99% of its energy within a diameter *d* of its center, where *d* is related to the spot size w_0 by [64]:

$$d = \pi w_{\mathrm{o}} \tag{4.11}$$

Therefore, by taking the null-to-null beam diameter of the Airy beam to be the diameter *d* for a Gaussian beam as described above, we can calculate the spot size w_0 of the Gaussian beam before the focusing lens L3.

A collimated Gaussian beam, of spot size w_0, passing through a lens with focal length f, has a spot size w_{foc} at the focus given by [64]

$$w_{\mathrm{foc}} = \frac{f\lambda}{\pi w_0} \tag{4.12}$$

We would like to emphasize that the spot size above is the radial distance from the beam axis at which the field amplitude falls to $1/e$ of its value at the waist.

In line with a common practice in nonlinear optics, we calculate the peak intensity using the 3 db spot size, i.e, the radial distance $r_{3\mathrm{db}}$ from the waist where the beam intensity reduces by 50%. We use the $1/e$ spot size, w_{foc}, in Equation (4.12) above to find the 3db spot size. After a simple calculation, we obtain

$$r_{3\mathrm{db}} = \sqrt{\frac{-\ln(0.5){w_{\mathrm{foc}}}^2}{2}} \tag{4.12}$$

We can finally calculate the intensity I_0 as

$$I_0 = \frac{P_{\mathrm{peak}}}{\pi {r_{3\mathrm{db}}}^2} \tag{4.12}$$

which can be used in Equations (4.6) and (4.10) to calculate the $n_{2(\mathrm{eff})}$ and $\beta_{(\mathrm{eff})}$.

As a final comment, we note that the theoretical open and closed aperture signals for our experimental set-up were calculated using a computer code which had been previously developed in our research group. The theoretical modelling is based on the Fresnel-Kirchoff diffraction integral [63]. We fit the theoretical curves to our experimental data to extract the values of Φ_{n2} and Φ_{β}.

4.3 Results and Discussion

We present measurements of the open aperture signal for our sample at several wavelengths, and we then extracted β values from it. In doing so, we do take into account the wavelength dependent transmission of the beam splitter BS1, due to which the average input power is different at different wavelengths. Figure 4.6 shows the open aperture data measured at different wavelengths, λ, ranging from 1180 nm to 1480 nm. As mentioned before, the z values in our experimental plots are not indicative of the distance from the focus, since our motorized stage was not calibrated with respect to the focal plane.

We observe that at λ = 1180 nm, the open aperture signal shows a peak. This indicates saturable absorption in the medium and hence a negative value of $\beta_{(\text{eff})}$. As the wavelength is increased to λ = 1260 nm, the open aperture signal shows a null response. This indicates that $\beta_{(\text{eff})}$ vanishes at this wavelength.

As the wavelength is further increased from λ = 1260 to 1380 nm, the open aperture signals show an increasingly strong dip. Hence there is an increasingly strong reverse saturable absorption, and $\beta_{(\text{eff})}$ is positive and grows monotonically in this wavelength region.

From λ = 1380 nm onwards, the dip in the open aperture signal becomes monotonically weaker, so much so that we observe a null in the open aperture signal at λ = 1440 nm. This indicates that β_{eff} decreases from a large positive value to zero in this wavelength range. Finally, we observe that the open aperture signal shows a peak at $\lambda = 1480$ nm, which indicates saturable absorption and a negative $\beta_{(\text{eff})}$.

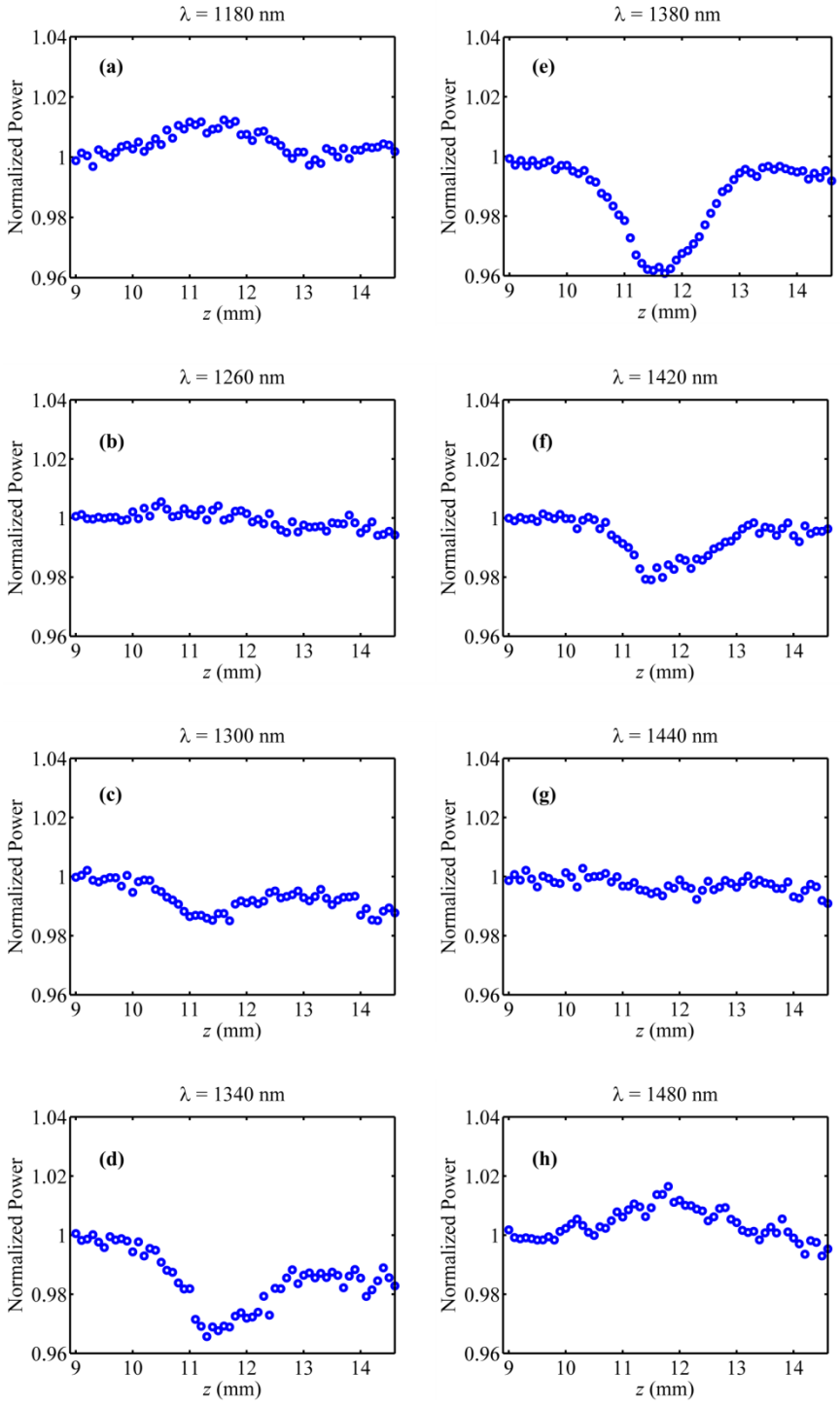

Figure 4.6: Measured open aperture transmission for several wavelengths λ.

Figure 4.7 shows the extracted values of $\beta_{(\text{eff})}$ from the open aperture data for λ = 1180 to 1480 nm. The results corroborate with our discussion above, and show how $\beta_{(\text{eff})}$ goes from negative to highly positive and then back to negative again. Importantly, $\beta_{(\text{eff})}$ takes on extremely large values, which are two orders of magnitude greater than the values reported for a bare ITO film [55], and three to five orders of magnitude larger than the values reported for many other nonlinear materials.

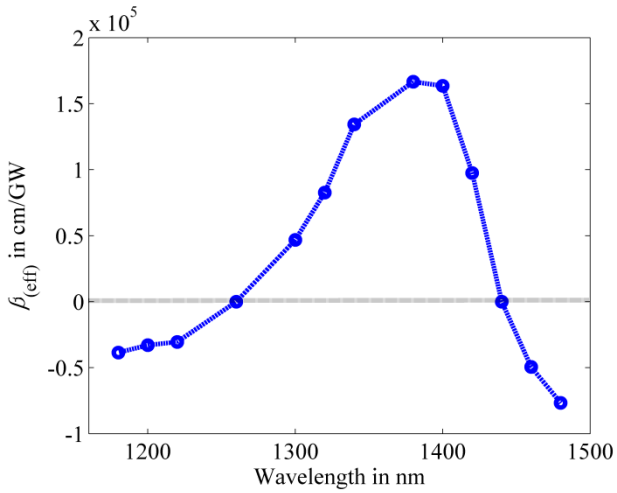

Figure 4.7: Calculated values of β_{eff} for different wavelengths using the method described above. The black dotted line shows where β_{eff} becomes zero.

Due to some experimental issues, the author was not able to perform accurate measurements for the closed aperture signal by the time of writing this thesis. Therefore, closed aperture measurements and the subsequent analysis of the n_2 values for the antenna-on-ITO structure are not presented here. However, preliminary measurements performed by our group have shown that the intensity-dependent refractive index, n_2, of the antenna-on-ITO structure is also extraordinarily large.

It is evident that the presence of plasmonic antennas greatly enhances the already-strong nonlinear optical response of ITO. The study reported in this chapter is currently continuing, and we hope to reach definitive conclusions about the specifics that enable the antenna-on-ITO structure to demonstrate such extraordinarily large optical nonlinearities.

Chapter 5

Conclusions and Outlook

In the course of this Master's thesis, the author completed two projects and contributed to a third ongoing project. The findings of these projects make significant contributions to the field of Photonics, and have the potential for a wide range of applications.

The first study presents principles for efficient design of plasmonic half-wave plates using L-shaped nanoantenna arrays. The principles reported therein enable more effective design of ultrathin waveplates using L-shaped nanoantenna arrays. This is important because designing nanophotonic components is often time intensive, and the results we present can serve as a guide towards achieving design goals tailored to available fabrication processes. However, the significance of this study goes far beyond what has been described above. The discussions we present are instructive in nature, and enable the reader to develop insights into the Physics of L-shaped nanoantenna arrays. The usefulness of this is not just restricted to the design of waveplates. The rich set of parameter space of L antennas has helped to realize optical phased arrays, which in turn have added new dimensions to the potency of light through phenomena such as anomalous refraction [39]. In addition, the planar structure of these antennas makes it easy to incorporate them in two-dimensional arrays. This enables to realize metasurfaces composed of these antennas with relative ease. Consequently, L-shaped nanoantennas have been proposed as building blocks for plasmonic metasurfaces. In addition, the insights we present in our study can be easily applied to a variety of other plasmonic structures which support orthogonal dipolar resonances. They can also serve as an inspiration to design and utilize more complex plasmonic scatterers.

The other two projects reported in this thesis deal with the investigation of a very exciting photonic material, i.e indium tin oxide (ITO), which demonstrates an extraordinarily large optical nonlinearity with an ultrafast response around its epsilon-near-zero (ENZ) wavelength [55]. Since ITO is lossy around its ENZ wavelength, it is not suitable for use in nonlinear optical devices involving long propagation lengths. However, it is suitable for use in compact, nanoscale nonlinear optical devices involving short propagation lengths. An example of such a device could be an ultrathin absorber, whose absorption is dynamically controlled by a control beam.

Moreover, since ITO is a non-stoichiometric material, its ENZ wavelength can be varied significantly. Therefore, the exciting possibilities described above can be realized over a broad range of wavelengths with proper doping of the ITO.

Surface plasmon modes often have short propagation lengths. Moreover, plasmonic structures enhance fields in the region around them. It therefore seems conducive to use plasmonic structures with ITO to further enhance the nonlinearity. The author thus undertook a study motivated by the use of plasmonic dipole antennas to enhance the already strong nonlinear optical response of ITO. Specifically, we considered a thin ITO film of 23 nm thickness for applications to ultrathin plasmonic metasurfaces.

Measurements of the linear optical response of the antenna-on-ITO structure were intriguing enough to constitute a separate study which we present in chapter 3. We report an unconventional optical response of plasmonic dipole antennas on the ITO substrate, which is characterized by dual resonances whose spectral locations are largely independent of the antenna dimensions. We conduct an elaborate analysis to demonstrate that the unconventional optical response arises due to coupling of the antenna resonance and the so-called ENZ mode of the thin ITO film. The ENZ mode supports very strong field enhancements in thin films around their ENZ wavelength, which shows huge promise to enhance the already strong nonlinearity of the ITO film. It is important to note that bound ENZ modes, which enable confined, enhanced fields within thin films, are not excited under normal incidence. However, the presence of plasmonic antenna provides the necessary momentum matching to excite the bound ENZ mode even when the structure is illuminated by normal incidence.

In chapter 4, we report an ongoing study of the nonlinear optical response of the antenna-on-ITO structure. We provide a comprehensive description of the experimental method based on the z-scan technique. The instructive nature of this description would serve to educate the reader about a broad range of concepts involved. The author performed measurements to characterize the intensity-dependent attenuation coefficient β, and the results show an enhancement of a factor of 100 as compared to β of bare ITO reported by Alam et al [55]. Due to experimental issues, the author could not perform measurements of the intensity-dependent refractive index n_2 at the time of writing this thesis. However, preliminary measurements by other participants of the project show an enhancement in n_2 by a factor of 1000, as compared to that of the bare ITO. It is

clear that the presence of the dipole antennas contributes to enhancing the nonlinearity of ITO. However, at the time of writing this thesis, we cannot make definitive statements about the specifics that enable this large optical nonlinearity. The completed results of this study will appear in published form in due course.

We observe here a beautiful blend of three seemingly independent areas of research: ENZ materials science, plasmonics and nonlinear optics. The presence of plasmonic antennas on an ITO substrate helps excite the bound ENZ mode even under normal incidence, thereby allowing field enhancements in the structure much larger than those observed for a plasmonic antenna on a conventional substrate like glass. The field enhancement, in turn, enhances the already strong nonlinear optical response of ITO. This thesis is thus unique in presenting studies which bring together three different fields of active research. As such, the work presented in this thesis has the potential to advance all these three fields, and is thus relevant to a broad spectrum of optical scientists.

References

1. A. F. Koenderink et al, “Nanophotonics: Shrinking light-based technology”, Science, Vol. 348, 2015.
2. M. Born et al, “Principles of Optics”, 7th edition, Cambridge University, 1999.
3. S. A. Maier, “Plasmonics: Fundamentals and Applications”, Springer, 2007.
4. P. Berini, “Long-range surface plasmon polaritons”, Advances in Optics and Photonics, Vol. 1, 2009.
5. D. K. Gramotnev et al, “Plasmonics beyond the diffraction limit”, Nature Photonics, Vol. 4, 2010.
6. P. Berini, “Plasmon-polariton waves guided by thin lossy metal films of finite width: Bound modes of asymmetric structures”, Physical Review B, Vol. 63, 2001.
7. P. N. Prasad, “Nanophotonics”, John Wiley and Sons, Inc., 2004.
8. V. Giannini et al, “Plasmonic Nanoantennas: Fundamentals and Their Use in Controlling the Radiative Properties of Nanoemitters”, Chemical Reviews, Vol. 111, 2011.
9. K. M. Mayer et al, “Localized Surface Plasmon Resonance Sensors”, Chemical Reviews, Vol. 111, 2011.
10. N. Meinzer et al., “Plasmonic meta-atoms and metasurfaces”, Nature Photonics, Vol. 8, 2014.
11. L Marucci et. al, “Optical spin-to-orbital angular momentum conversion in inhomogeneous anisotropic media”, Physical Review Letters, Vol. 96, 2006.
12. A Papakostas, et.al, “Optical manisfestations of planar chirality”, Physical Review Letters, Vol. 90, 2003.
13. Y. Zhao et al, “Twisted optical metamaterials for planarized, ultrathin, broadband circular polarizers”, Nature Communications, Vol. 3, 2012.
14. J. K. Gansel et al, “Gold helix photonic metamaterial as broadband circular polarizer”, Science, Vol. 325, 2009.
15. N.B Khlebtsov et al,” Can the light scattering depolarization ratio of small particles be greater than 1/3?”, The Journal of Physical Chemistry B, Vol. 109, 2005.
16. C. Noguez et al, “Optical properties of elongated noble metal nanoparticles”, The Journal of Physical Chemistry C, Vol. 112, 2008.

17. Z. Gryczynski et al," Depolarized light scattering from silver nanoparticles", Chemical Physics Letters, Vol. 421, 2006.
18. Z. Gryczynski et al, "Interference of surface plasmon resonances causes enhanced depolarized light scattering from metal nanoparticles", Chemical Physics Letters, Vol. 434, 2007.
19. T. Shegai et al, "Managing light polarization via plasmon–molecule interactions within an asymmetric metal nanoparticle trimer", Proceedings of National Academy of Sciences USA, Vol. 105, 2008.
20. C. Hong-Ya et al, "Broadband perfect polarization conversion metasurfaces", Chinese Physics B, Vol. 24, No. 1, 2015.
21. P. Yu et al**,** "Generation of vector beams with arbitrary spatial variation of phase and linear polarization using plasmonic metasurfaces"**,** Optics Letters, Vol. 40, No. 14, 2015.
22. K. Iwami et al, "Ultrasmall radial polarizer array based on patterned plasmonic nanoslits", Applied Physics Letters, Vol. 101, 2012.
23. X. Chen et al, "Dual-polarity plasmonic metalens for visible light ", Nature Communications, Vol. 3, 2012.
24. L. Young et al, "Meander-line polarizer", IEEE Transactions on Antennas and Propagation, Vol. 21, 1973
25. R. D Averitt et al, "Comparison of birefringent electric split-ring resonator and meanderline", Optics Express, Vol. 17, 2009.
26. S. L. Wadsworth et al, "Broadband circularly-polarized infrared emission from multilayer metamaterials", Optical Materials Express, Vol. 1, 2011.
27. T. Li et al, "Manipulating optical rotation in extraordinary transmission by hybrid plasmonic excitations", Applied Physics Letters, Vol. 93, 2008.
28. A. Pors, "Plasmonic metamaterial wave retarders in reflection by orthogonally oriented detuned electrical dipoles", Optics Letters, Vol. 36, No. 9 , 2011.
29. Y. Zhao et al, "Tailoring the dispersion of plasmonic nanorods to realize broadband optical meta-waveplates", Nano Letters , Vol. 13, 2013.
30. J. Shao, "Polarization conversions of linearly and circularly polarized lights through a plasmon-induced transparent metasurface", Journal of Applied Physics, Vol. 115, 2014.

31. W. Chen, “Large-area nanoimprint colloidal Au nanocrystal-based nanoantennas for ultrathin polarizing plasmonic metasurfaces”, Nano Letters, Vol. 15, 2015.
32. Z. H. Jiang, “Broadband and wide field-of-view plasmonic metasurface-enabled waveplates”, Scientific Reports, Vol. 4, 2014.
33. S. C. Jiang, “Controlling the polarization state of light with a dispersion-free metastructure,” Physical Review X, Vol. 4, 2014.
34. F. Ding , “Broadband high-efficiency half-wave plate: a supercell-based plasmonic metasurface approach”, ACS Nano, Vol. 9, 2015.
35. Q. Xu, “Fabrication of large-area patterned nanostructures for optical applications by nanoskiving,” Nano Letters, Vol. 7, 2007.
36. J. Sung, “Nanoparticle spectroscopy: birefringence in two-dimensional arrays of L-shaped silver nanoparticles,” Journal of Physical Chemistry C, Vol. 112, 2008.
37. N. Yu, “A broadband, background-free quarter-wave plate based on plasmonic metasurfaces,” Nano Letters, Vol. 12, 2012.
38. L.-J. Black, “Optimal polarization conversion in coupled dimer plasmonic nanoantennas for metasurfaces,” ACS Nano, Vol. 8, 2014.
39. N. Yu, “Light propagation with phase discontinuities: generalized laws of reflection and refraction,” Science, Vol. 334, 2011.
40. E. Karimi et al, “Generating optical orbital angular momentum at visible wavelengths using a plasmonic metasurface,“ Light: Science and Applications, Vol. 3, e167 2014.
41. F. Bouchard et al, “Optical spin-to-orpital angular momentum conversion in ultra-thin metasurfaces with arbitrary topological charges,”, Applied Physics Letters, Vol. 105, 2014.
42. R. Blanchard et al, “Modeling nanoscale V-shaped antennas for the design of optical phased arrays,” Physical Review B, Vol. 85, 2012.
43. H. Gudjonson, “Accounting for inhomogeneous broadening in nano-optics by electromagnetic modeling based on Monte Carlo methods,” Proceedings of National Academy of Sciences USA, Vol. 111, 2013.
44. D. M. Sullivan, “Electromagnetic simulation using the FDTD method”, IEEE Press Series, 2000.
45. https://www.lumerical.com/

46. P. B. Johnson, “Optical constants of the noble metals”, Physical Review B, Vol. 6, 1972
47. E. D. Palik, “Handbook of optical constants of solids”, Academic Press, 1997.
48. I. Romero, “Plasmons in nearly touching metallic nanoparticles: singular response in the limit of touching dimers”, Optics Express, Vol. 14, 2006.
49. Nader Engheta, “Materials science. pursuing near-zero response”, Science, Vol. 340, 2013
50. C. Argyropoulos, et al, “Boosting optical nonlinearities in ε-near-zero plasmonic channels”,

Physical Review B, Vol. 85, 2012.

51. M. G. Silveirinha et al, “Transporting an image through a subwavelength hole”, Physical Review Letters, Vol. 102, 2009.
52. A. Capretti et al, “Enhanced third-harmonic generation in Si-compatible epsilon-near-zero indium tin oxide nanolayers”, Optics Letters, Vol. 40, 2015.
53. R. Fleury et al, “Enhanced superradiance in epsilon-near-zero plasmonic channels”, Physical Review B, Vol. 87, 2013.
54. M. A. Vincenti et al, “Singularity-driven second- and third-harmonic generation at ε-near-zero crossing points”, Physical Review A, Vol. 84, 2011.
55. M. Z. Alam, et al, “Unprecedentedly large optical nonlinearity of indium tin oxide in its epsilon-near-zero region”, Science, Vol. 352, 2016.
56. A. D. Boardman, “Electromagnetic Surface Modes”, Wiley, New York, 1982.
57. Simon Vassant et. al, “Berreman mode and epsilon near zero mode”, Optics Express, Vol. 20, No. 21, 2012.
58. Salvatore Campione et al, “Theory of epsilon-near-zero modes in ultrathin films”, Physical Review B, Vol. 91, 2015.
59. T. Taliercio et al, “Brewster mode in highly doped semiconductor layers: an all-optical technique to monitor doping concentration”, Optics Express, Vol. 22, No. 20, 2014.
60. R. W. Boyd, “Nonlinear Optics”, 3rd edition, Academic Press, 2008
61. H. S. Nalwa & S. Miyata, “Nonlinear Optics of Organic Molecules and Polymers”, CRC Press, 1997.
62. M. Sheik-Bahae, “Sensitive measurements of optical nonlinearities using a single beam”, IEEE Journal of Quantum Electronics, Vol.26, No. 4, 1990.

63. B. Yao et al, “Z-scan theory based on a diffraction model”, Journal of Opitcal Society of America B, Vol. 20, No. 6, 2003.
64. A. Siegman, “Lasers”, University Science Books, 1986.